Journal of the Mechanics and Physics of Solids 61 (2013) 762–782

Contents lists available at SciVerse ScienceDirect

Journal of the Mechanics and Physics of Solids

journal homepage: www.elsevier.com/locate/jmps

A distinct element method for large scale simulations of carbon nanotube assemblies

Igor Ostanin [a], Roberto Ballarini [a], David Potyondy [b], Traian Dumitrică [c,*]

[a] Department of Civil Engineering, University of Minnesota, 500 Pillsbury Drive S.E., Minneapolis, MN 55455, United States
[b] Itasca Consulting Group, Inc., 111 Third Avenue South, Minneapolis, MN 55401, United States
[c] Department of Mechanical Engineering, University of Minnesota, 111 Church Street S.E., Minneapolis, MN 55455, United States

ARTICLE INFO

Article history:
Received 29 April 2012
Received in revised form
17 August 2012
Accepted 31 October 2012
Available online 15 November 2012

Keywords:
Distinct element method
Carbon nanotubes
Van der Waals interactions

ABSTRACT

Mesoscale simulation techniques are becoming increasingly important due to the interest in complex mechanical problems involving nanomaterials. We propose applying the established macroscopic modeling concept of distinct spherical elements down to the mesoscale to simulate mechanical behavior of carbon nanotube systems. Starting from a microscopic description, the important interactions are encapsulated into two types of contact models that act simultaneously. Each individual nanotube is coarse-grained into a chain of spherical elements interacting by parallel-bonded contacts, representing the short-ranged covalent bonding. An anisotropic van der Waals model with aligning moments acts at the contact between elements located in different tubes to represent the long-ranged interactions. The promising potential of the proposed methodology to model large scale carbon nanotube assemblies is illustrated with several examples, including self-folding of individual nanotubes, mechanical testing of nanotube ropes, self-assembly of a high-porosity nanotube paper, and mechanical testing of a low-porosity nanotube paper.

1. Introduction

Carbon nanotubes (Iijima, 1991) (CNTs) possess mechanical and physical properties that render them attractive for numerous technological applications. Their promise, however, can be realized only through improved understanding of the mechanical, electrical and thermal properties not only of individual tubes but also bundles, ropes, papers and other CNT assemblies (Dalton et al., 2003; Filleter et al., 2012; Harris et al., 2012; Hobbie et al., 2010; Hutchens et al., 2012; Shuba et al., 2012).

Valuable insights into individual CNT mechanics have been obtained from microscopic simulations (Dumitrică et al., 2003, 2006; Dumitrică and Yakobson, 2004; Jeong et al., 2007; Nikiforov et al., 2010; Zhang et al., 1998, 2009) using techniques like molecular dynamics (MD). Unfortunately, performing exhaustive simulations at the atomistic scale for CNT systems of scientific and engineering significance remains computationally prohibitive. Therefore, mesoscopic approaches have been developed to make simulations of CNT systems manageable (Buehler, 2006; Cranford and Buehler, 2010; Hahm et al., 2012; Huang et al., 2008; Liba et al., 2008; Shi et al., 2008; Volkov et al., 2008; Volkov and Zhigilei, 2010a, 2010b, 2010c; Xie et al., 2011; Zhigilei et al., 2005; Zou et al., 2009; Wang et al., 2012). Two such mesoscopic models have gained

* Corresponding author. Tel.: +1 612 625 3797; fax: +1 612 624 5230.
E-mail addresses: broberto@umn.edu (R. Ballarini), dtraian@me.umn.edu, td@me.umn.edu (T. Dumitrică).

0022-5096/$ - see front matter © 2012 Elsevier Ltd. All rights reserved.
http://dx.doi.org/10.1016/j.jmps.2012.10.016

popularity—the *bead-and-spring* (BS) model (Buehler, 2006; Cranford and Buehler, 2010; Hahm et al., 2012; Xie et al., 2011) and the *mesoscopic-force-field* (MFF) model (Volkov et al., 2008; Volkov and Zhigilei, 2010a, 2010b, 2010c; Zhigilei et al., 2005). Nevertheless, in spite of such developments, simulations of collective CNT behavior have not kept pace with the demand from many areas ranging from nanoelectromechanical systems, nanocomposite materials, mechanical energy storage, or nanotoxicology.

The BS model was appropriated from the coarse-grained modeling of organic polymers (Rouse, 1953; Underhill and Doyle, 2003; Zimm, 1956). As the name suggests, a CNT is represented by a collection of point masses connected by linear springs. Simulations based on BS model were successfully carried out to study various behaviors of hundreds of CNTs on a timescale approaching microseconds (Buehler, 2006). The MFF model describes the motion of a CNT in terms of the dynamics of nodal point masses, connected by flexible cylinders. The advanced features of the numerical method developed on this model are the adaptive meshing technique that allows reduction in the number of degrees of freedom, and the physically realistic potential of van der Waals (vdW) dispersive interactions.

Modeling CNT systems requires accurate accounting for both covalent and vdW forces. It is beyond the scope of this paper to review the coarse graining schemes of these forces employed in the BS and MFF models. It is however important to recognize that any coarse graining procedure should agree with the microscopic description or experiment in the features deemed important for the problem at hand. For example, it is known from experiment that in metallic and semiconducting CNT films, the constituent CNTs form large close-packed bundles (Thess et al., 1996; Hobbie et al., 2010; Harris et al., 2012), which are entangled, Fig. 1. This self-organization is attributed the vdW interactions among CNTs. Attempts to simulate the bundling process with the two methods applied to an identical CNT film configuration led to different outcomes (Volkov et al., 2008): While the configuration evolved using the BS model remained organized in randomly oriented individual CNTs and small bundles of just few CNTs, the MFF simulation obtained large bundles composed of approximately 50–100 CNTs, in agreement with experimentation (Harris et al., 2012; Hobbie et al., 2010). This qualitatively different behavior can be attributed to the way in which the long-range vdW interaction between CNTs is being captured in the two mesoscopic models. While in the BS model the intertube interaction is modeled with a spherically symmetric potential associated with pairs of beads, the same interaction is described more realistically in MFF by considering the vdW coupling of cylindrical elements of arbitrary lengths and orientations (Volkov and Zhigilei, 2010a). Similarly, in the work by Volkov and Zhigilei (2010a), the BS model was used to generate self-equilibrated specimens of CNT film. The obtained film structure exhibited bundles composed of just few CNTs.

Recently, we proposed (Anderson et al., 2010) *distinct-element-method* (DEM) modeling of CNTs. DEM, the macroscopic method introduced by Cundall and Strack (1979, 1988), and Hart et al. (1988) more than 30 years ago, was developed for simulating the mechanical properties and response of macroscopic geological materials (Pande et al., 1990) and structures by representing them as a large numbers of interacting rigid spherical particles. In DEM, a CNT is therefore represented by a chain of rigid spherical particles interacting with each other via prescribed contact models informed by the results obtained from simulations at the atomistic scale. Existing and available robust procedures for identifying the particles in contact (Cundall and Strack, 1988), stable time integration scheme (Hart et al., 1988) and great versatility and popularity of existing codes (Itasca CG Inc., 2008) are convincing arguments for further developing a DEM-based mesoscopic model for CNTs. By solving the technical aspects related with encapsulating the long-range microscopic vdW interaction into a vdW contact model, in this paper we enable large-scale simulations of CNT systems and place DEM as an advanced alternative methodology to the existing approaches. With respect to BS, MFF and other mesoscopic models (Liba et al., 2008; Wang et al., 2012), the main conceptual advances here are the treatment of the spherical particles as rigid bodies and the coarse

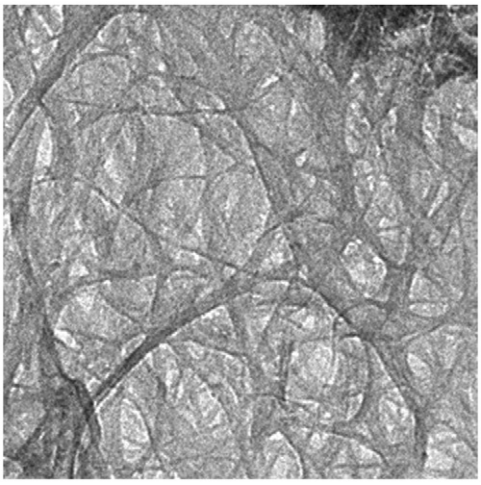

Fig. 1. A CNT semiconducting film imaged with TEM, showing the organization of constituent single-wall CNTs into large bundles. Vertical and horizontal sizes of the image represent 500 nm. (Image courtesy E. Hobbie.)

graining of the microscopic covalent and vdW forces into contact models leading to both moments and forces acting on the coarse grained spherical particles. The importance of these features is discussed in the presented example simulations.

While sharing the particle-discretization-of-the-continuum basis with other macroscopic methods, such as smoothed particle hydrodynamics (Gingold and Monaghan, 1977; Desbrun and Gascuel, 1996; Hoover, 2006) or materials point method (Sulsky et al., 1994), DEM is generally distinguished by the explicit accounting for the rotational degrees of freedom of particles (considered to be spherical or more complicated geometries, depending on the application) as well as by the introduction of the contact laws between particles. At the mesoscale, DEM was previously used to model powders in which each particle is considered to be either a whole or a part of a granular medium (Dutt et al., 2005) and also to model rock in which the particles and contacts are considered to be grains and cement, respectively (Potyondy and Cundall, 2004). To our knowledge, this is the first time when the method is used to model CNT systems. Furthermore, the model developed here could be further adapted to simulate deformation of other more complex semi-flexible random fiber networks encountered in biological and nonliving systems (Hatami-Marbini and Picu, 2009).

2. Distinct element method for CNTs

DEM is a technique that computes the damped dynamics of a collection of interacting classical spherical particles with uniformly distributed mass m and moment of inertia I. The state variables for each particle include position, translational velocity, and angular velocity. Specifically, the translational motion of the center of mass of a particle is described in terms of its position $\mathbf{x}$ and velocity $\mathbf{v}$. The rotational motion is monitored by the angular velocity $\boldsymbol{\omega}$. The dynamics is described by laws of classical mechanics

$$\begin{aligned}\mathbf{F} &= m\ddot{\mathbf{x}},\\ \mathbf{M} &= I\dot{\boldsymbol{\omega}},\end{aligned} \tag{1}$$

where $\mathbf{F}$ and $\mathbf{M}$ are the resultant force and moment vectors that arise from the interaction of a particle with other elements. To solve these equations numerically, an artificial dissipative damping (for both force and moment equations), referred to as local damping in Itasca CG Inc. (2008), is also introduced for the purpose of stabilizing the assemblies of moving particles under external load, and for relaxing the system into a metastable state. The magnitude of each component of the damping force and moment is proportional to the corresponding component of the resultant force and moment, and they act in a direction to oppose the corresponding velocity and angular velocity. The proportionality constant ξ, referred to as the local-damping constant, ranges from 0 to 0.7. Only accelerated motion is being damped.

In our scheme, Eqs. (1) are solved using an explicit leapfrog finite difference algorithm involving a timestep Δt. According to this scheme, translational and rotational velocities are iterated at the mid-interval, from $t-0.5\Delta t$ to $t+0.5\Delta t$ as

$$\begin{aligned}\mathbf{v}(t+0.5\Delta t) &= \mathbf{v}(t-0.5\Delta t)+\frac{\mathbf{F}(t)}{m}\Delta t,\\ \boldsymbol{\omega}(t+0.5\Delta t) &= \boldsymbol{\omega}(t-0.5\Delta t)+\frac{\mathbf{M}(t)}{I}\Delta t.\end{aligned} \tag{2}$$

The position of a particle is iterated from t to $t+\Delta t$ as

$$\mathbf{x}(t+\Delta t) = \mathbf{x}(t)+\mathbf{v}(t+0.5\Delta t)\Delta t. \tag{3}$$

The timestep Δt is dynamically adjusted to ensure the stability of the scheme ((2), (3)). While the above algorithm does not provide a thermodynamic integration like in coarse-grained MD approaches (Buehler, 2006; Zhigilei et al., 2005), it is known to work very well for larger scale mechanical simulations.

The forces and moments on each interacting particle are derived from a contact model prescribed in advance. Various contact models of mechanical nature are already in place (Itasca CG Inc., 2008) permitting for DEM macroscopic simulations in various areas of science and engineering. Compelled to apply DEM at the nanoscale, we proposed (Anderson et al., 2010) a mesoscopic CNT model consisting of a chain of spherical particles whose interaction is dictated by a standard parallel bond contact (Potyondy and Cundall, 2004) and a special van der Waals contact. In the following we give a concise overview of this model and illustrate its application to a (10,10) CNT.

We homogenize an undeformed CNT into a cylindrical shell with finite thickness (Fig. 2) and partition it into identical mass representative elements (REs) of finite lengths T. Each spherical particle represents a mass RE. As an example, in Table 1 we chose to partition a (10,10) CNT with diameter $2r_{CNT} = 13.560$ Å into mass REs with $T = 2r_{CNT}$. This way, each mass RE contains approximately 220 carbon atoms. Parameters m and I are equal with the mass and moment of inertia of a cylindrical RE taken with respect to the CNT long axis. It follows that the spherical particle has a radius

$$r = \sqrt{2.5}r_{CNT}. \tag{4}$$

The spherical particles are equispaced at a distance T apart. Their centers are located on the CNT long axis.

Although the focus of this paper is a hierarchical multiscale modeling of CNT systems, a hybrid atomistic-DEM multiscale modeling based on this framework can be imagined at this stage. Coarse grained spherical elements can be coupled with explicit atomistic modeling that model regions with high local strains, where nonlinear deformations or fracture may develop. To facilitate this development, the REs may be selected as an integer number of repetitive translational units of the intrinsic CNT lattice. In addition, the representation of a translational unit could be changed in the

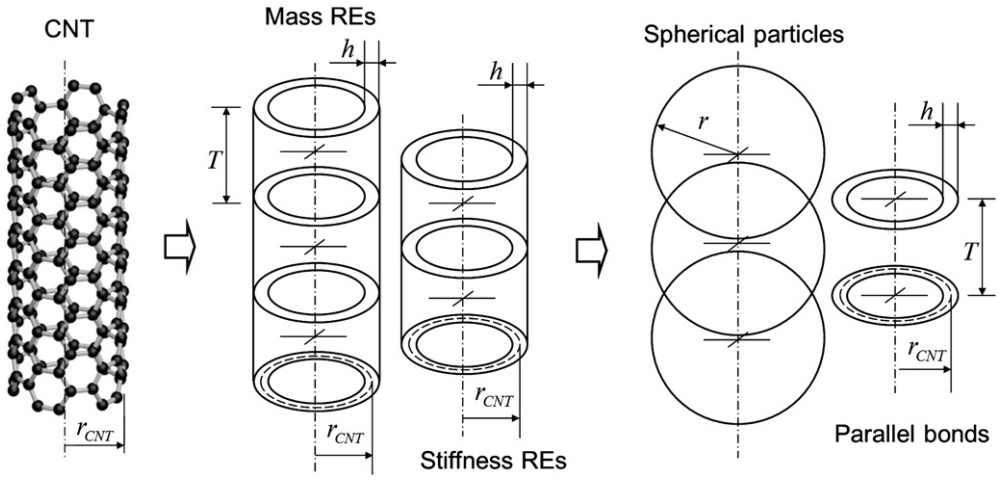

Fig. 2. Coarse graining of a CNT into cylindrical mass and stiffness representative elements (REs). The inertial and elastic properties of REs are lumped into the collection of spherical particles and parallel bonds.

Table 1
Parameterization of the spherical particles and parallel bonds for a (10,10) CNT. m, r, I are the mass, radius, moment of inertia of each spherical particle. T is the interparticle spacing. $\overline{A}$, $\overline{I}$ and $\overline{J}$ are the interface cross section area, moment of inertia and polar moment of inertia respectively. The normal k_n and shear k_s stiffness (measured per unit area) are based on microscopically computed Young's $Y=1029$ GPa and shear $G=459$ GPa elastic constants.

m (amu)	r (Å)	I (amu × Å^2)	T (Å)	$\overline{A}$ (Å^2)	$\overline{I}$ (Å^4)	$\overline{J}$ (Å^4)	k_n (eV/Å^4)	k_s (eV/Å^4)
2649	10.72	1.218×10^5	13.56	142.7	3480	6960	0.474	0.211

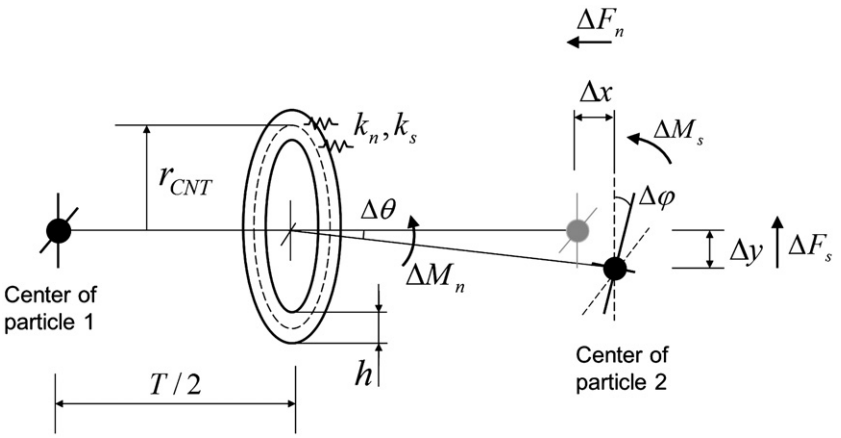

Fig. 3. Detail showing a parallel bond interface located halfway between the centers of two spherical particles and the restoring forces and moments developed in response to relative displacements.

course of the simulation, from the coarser spherical element to the finer atomistic level or vice versa. The treatment of the spherical particles as rigid bodies and thus the knowledge of the relative displacements and angular orientations between the spherical elements keeps open the possibility of performing a reverse spherical DEM element-atomistic mapping (Ensing and Nielsen, 2010).

The linking of the microscopic deformations to that of the mesoscopic model is performed here using the phenomenology of elastic continuum. We idealized the CNT wall as an isotropic elastic shell of thickness $h=3.35$ Å with prescribed density and elastic constants. Young's (Y) and shear (G) elastic moduli associated with this shell are obtained from accurate atomic-level simulations (Zhang and Dumitrică, 2008). The shell is partitioned into REs of length T that are located in between the centers of the spherical particles. The elastic constants of an elastic RE are lumped into a parallel bond contact between the neighboring particles. These bonds, formed between any two neighboring particles in the chain of spherical particles representation of the CNT, can be imagined as flat interfaces of hollow circular cross sections (Fig. 3).

They contain uniformly distributed linear springs with normal k_n and shear k_s stiffness (measured per unit area) representing the elastic response of an RE of length T. These stiffness are

$$k_n = Y/T,$$
$$k_s = G/T. \tag{5}$$

When the contact is formed in the straight CNT, the total contact forces and moments are initialized to zero. The deformation of the chain of bonded elements under external loads results in nodal displacements in generalized coordinates (Fig. 3), describing relative stretch (Δx), shear (Δy), bending angle ($\Delta\theta$) and torsion ($\Delta\varphi$). The restoring contact forces (normal force ΔF_n and shear force ΔF_s) and moments (bending moment ΔM_n and twisting moment ΔM_s) are developed according to the incremental laws

$$\Delta F_n = -k_n \overline{A} \Delta x,$$
$$\Delta F_s = -k_s \overline{A} \Delta y,$$
$$\Delta M_n = -k_n \overline{I} \Delta\theta.$$
$$\Delta M_s = -k_s \overline{J} \Delta\varphi. \tag{6}$$

Here $\overline{A}$, $\overline{I}$ and $\overline{J}$ are the interface cross section area, moment of inertia and polar moment of inertia respectively. The parallel bond was originally introduced as an interface of circular cross section, an approximation that is suitable for multi-walled CNTs with closed core (Anderson et al., 2010). For the case of single-walled CNTs, we adjusted the contact to a hollow circular cross section. Then, the area, moment of inertia, and polar moment of inertia associated with the parallel bond are

$$\overline{A} = 2\pi h r_{CNT},$$
$$\overline{I} = \pi h r_{CNT}(r_{CNT}^2 + 0.25h^2),$$
$$\overline{J} = 2\overline{I}. \tag{7}$$

Up to this point the development of the mesoscopic model has been pursued by a straightforward appropriation of the macroscopic DEM methodology. With the minimal parallel bond contact model that captures the short-ranged covalent binding of C atoms, one can study the deformations and acoustic vibrations of an individual realistic CNT. Table 1 gives the parametrization of inertial and elastic properties of a (10,10) CNT. In most application CNTs are present in the form of ropes, cables, and papers. Their collective mechanical behavior originates not only on the covalent but also weak van der Waals (vdW) C-C interactions, that build up over extended contacts. To make the DEM methodology viable for such simulations, the main challenge is to derive a contact model that can efficiently capture these non-bonding vdW interactions between CNTs.

We now introduce such a vdW contact model, which will lead to additional forces and moments acting on the collection of spherical particles. Broadly, physical theories of van der Waals forces can be generally separated into two camps: microscopic and macroscopic theories. The microscopic theory is a bottom-up approach based on the atom–atom dispersion interaction of London (1930), in which the total interaction is thought of as a sum of contributing part of the microscopic constituents. Under the assumption of pairwise additivity, the microscopic dispersive interactions sum to describe the total interaction between mesoscopic or macroscopic bodies. In an opposite top-down fashion, macroscopic theories of Hamaker and Lifshitz (Dzyaloshinskii et al., 1961; Hamaker, 1937) start with the dispersive energy between macroscopic bodies. Again under the assumption of additivity, the effective microscopic contributions can be backed out of these theories.

Here we base our model on a microscopic theory in which the interaction between two C atoms located on different CNTs is given by the standard Lennard-Jones (LJ) potential

$$v(d) = 4\varepsilon\left[\left(\frac{d_0}{d}\right)^{12} - \left(\frac{d_0}{d}\right)^{6}\right] \tag{8}$$

with parameters $d_0 = 3.851$ Å and $\varepsilon = 0.004$ eV. This interaction occurs only if the distance d between atoms is less than a cutoff radius parameter, which is typically chosen to be of the order of few nm. Assuming that atoms are uniformly distributed over the cylindrical surfaces of two interacting CNTs, Fig. 4(A), we can calculate the potential energy of interaction of two CNTs as

$$V = \rho^2 \int_{S_1}\int_{S_2} v(d)\, dS_1\, dS_2, \tag{9}$$

where S_1 and S_2 are the surfaces of first and second CNTs, $\rho = 4/(3\sqrt{3}a_{C-C}^2)$ is the area density of carbon atoms on a CNT surface (here $a_{C-C} = 1.42$ Å is the equilibrium carbon–carbon bond length). If two CNTs are crossed, the energy of interaction is finite, even in the case of infinite tubes. In the case of two parallel CNTs one can consider the interaction energy per unit length, considering the interaction between the finite RE of the first CNT with infinite second CNT, and normalizing the result with the RE length T. We build our coarse grained model under the requirement that this interaction energy, such as the one shown in Fig. 4(B), should be regained by summing the vdW contact energy among the REs located on the different CNTs. The proposed vdW contact model is a function of intercenter distance and the mutual orientation of REs. In the next section we describe the construction of this vdW contact model.

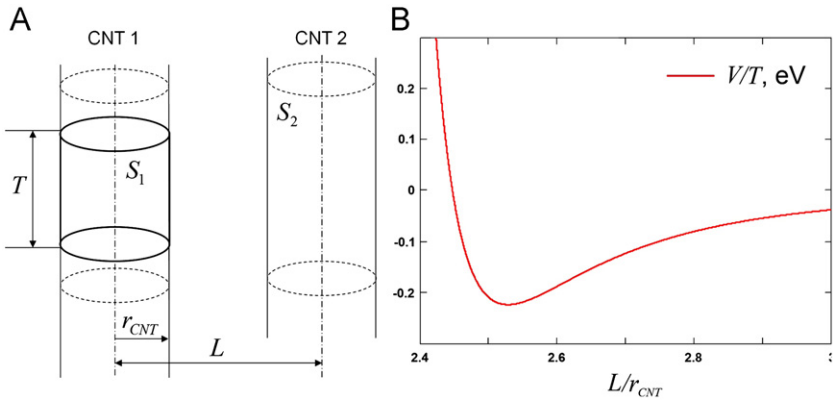

Fig. 4. (A) Schematics of two aligned infinitely long CNTs. (B) Plot of the interaction potential of two (10,10) parallel nanotubes (measured per length) as a function of the normalized intertube distance, as described by Eq. (10).

In DEM logic, the interaction between particles are incorporated using the concept of contact between distinct elements. To each spherical particle is associated a spherical distinct element such that when these elements overlap, a contact is formed. We note that the particle radius r resulting via our coarse graining procedure of a CNT (Fig. 2), may or may not lead to interpenetration. Nevertheless, this concept, designed for mechanical contact models, is used here to activate the interactions important at the nanoscale. To activate both the parallel bond and vdW contact models, we associate to each spherical particle a distinct spherical element, with radius equal to half the microscopic vdW interaction cutoff radius. Only nearest-neighbor spherical particles within the same CNT will form parallel bonds. By contrast, the vdW interaction typically involves one spherical particle from one CNT, in vdW contact with several spherical particles located on a second CNT. We emphasize that the role of these associated spherical distinct elements is only to activate the interactions and determine the forces and moments acting on the spherical particles with mass m and radius r.

3. Contact models for vdW interactions

3.1. An isotropic contact model of dispersive interactions

In the most general case of arbitrarily positioned CNTs, the integral (9) is too complex to be solved in closed form. However, assuming parallel and identical CNTs, Fig. 4(A), and taking the near limit, the integral takes a transparent analytical form (Anderson, 2010). The interaction energy per unit length writes

$$V(L)/T = 4\epsilon\left(\frac{A}{D^{\alpha}} - \frac{B}{D^{\beta}}\right). \tag{10}$$

Here, $D=(L/r_{CNT})-2$ is the normalized intertube center to center distance. The parameters of this potential are $\epsilon = 3\pi d_0^6\rho^2\varepsilon/8r_{CNT}^3$, $A = 21d_0^6 a/32r_{CNT}^6$, with the dimensionless constants $a\approx 0.41$ and $B\approx 1.31$. The plot of this potential for two (10,10) CNTs is given in Fig. 4(B). Note that the powers of D, $\alpha = 9.5$ and $\beta = 3.5$, are different from the ones of the microscopic LJ potential (8) and arise via the integration procedure (Anderson, 2010). The two terms in (10) have the evident repulsion and attraction meaning. It follows that this potential has an optimal intertube separation

$$L_0 = r_{CNT}\left[\left(\frac{\alpha A}{\beta B}\right)^{1/(\alpha-\beta)} + 2\right]. \tag{11}$$

In the following, Eq. (10) will serve as a reference for designing vdW contact models. As $V(L)$ captures the interaction energy between one RE segment of length T located on first the CNT and the second infinitely long CNT, Fig. 4(A), it becomes immediately clear that the total vdW interaction energy can be regained by summing the pair interaction between face-to-face REs of length T located on different CNTs. Thus, Eq. (10) suggests a naïve contact model in which each two aligned REs of length T located on different CNTs interact via the spherical symmetric vdW contact model $V(R)$, where R represents the distance between the centers of the spherical particles. It is evident that because the underlying integration has been performed with the CNTs being parallel, this model will be inappropriate for describing the interaction of the crossed CNTs. Nevertheless, this contact model introduces significant artifacts even when the tubes are parallel.

We illustrate the later deficiency with an example consisting of two interacting (10,10) CNTs of the length $L_{CNT} = 20.3$ nm represented by 15 identical spherical particles, such as the ones indicated in Table 1. Let V_{DEM} be the DEM model intertube potential energy defined as the superposition of all $V(R)f_c(R)$ pairwise contact interactions between the spherical elements of first and second CNT. The smooth cutoff function $f_c(R)$ (see Appendix) ensures the absence of energy jumps in the tube–tube potential, associated with cutoff radii of pair interactions.

Consider first the perfectly aligned case. The radius of the vdW distinct element was chosen $4r_{CNT}=2.71$ nm, which means that one RE located on one CNT interacts with few REs on the second CNT. Although the face-to-face first-neighbor contacts will bring the major contribution to V_{DEM}, there are non-negligible contributions from the second- and third-neighbor interactions. There is a quick remedy for this issue facilitated by the transparent $V(R)$ form. To restore $V_{DEM}(L)$ to the desired shape, we still used the functional form of $V(R)$ but the parameters A, ϵ, and β parameters slightly adjusted to match L_0, $V(L_0)$, and the far field scaling. The original and adjusted parameters of pair potential of interaction between segments of (10,10) tubes with length $T=2r_{CNT}$ are listed in the first and second line of Table 2, respectively.

Next, consider the interaction of misaligned CNTs. The coordinate z describes the misalignment of these adjacent CNTs, Fig. 5(A). The $V_{DEM}(L,z)$, plotted in Fig. 5(B), displays correct intertube spacing and binding energy at $z=0$. However, for misaligned configurations we note a corrugated relief with periodicity T. Of course, this periodic structure of the potential is an artifact of the model. Physically, it introduces unwanted high adhesive shear strength between two parallel CNTs and a preference for staggered (such as $z=T$) alignments. At this point, it is important to note that the unwanted corrugation artifact is an attribute of the spherical symmetry of the potential used in the contact model.

It should be mentioned that at the microscopic level, there is a real corrugation effect associated with the graphitic lattice structure of the tube walls and their registry. This effect was discarded in our vdW integration procedure in which atoms were uniformly distributed over cylindrical surfaces. We do not intend to capture this microscopic effect here, since the difference in energy between the maximum and minimum energies associated with this corrugation is small compared for example to the amount of vdW energy associated with bringing two tubes close to their optimal vdW separation (Carlson and Dumitrică, 2007). Unfortunately the staggering-induced corrugation becomes large for REs with large T, and it can significantly influence the outcome of a coarse grained simulation. As we already mentioned, these large artificial barriers prevent the long-range rearrangements of individual CNTs into continuous networks of bundles (Volkov et al., 2008). An *ad hoc* way to reduce the amplitude of this corrugation is to decrease T, thus to increase the number of particles representing the CNT (Anderson et al., 2010). However, this approach reduces the computational effectiveness of the methodology, making it unattractive for large-scale applications.

3.2. Anisotropic vdW contact model

The isotropic model (10) with parameters given in Table 2 provides the basis for developing a vdW contact model with the following attributes: (i) It has a simple analytical expression and (ii) captures short-range anisotropy to convey the form factors of cylinders and thus to correctly describe the shear interactions between parallel CNTs. (iii) Along with normal and shear forces, it includes moments that tend to align nanotube segments. More specifically, the new model incorporates two adjustments. Firstly, we consider interacting parallel segments and introduce an axial anisotropy of the contact that ensures the smoothness of the potential. Secondly, we introduce the adjustment related to aligning moments that are present in the case of non-parallel axes of the cylindrical segments. For both adjustments, we ensure correct far field behavior by introducing decay and smooth cutoff multipliers.

Table 2
Parameterization of the isotropic contact vdW model for the interaction between two (10,10) CNTs. The first line lists the value of the parameters as obtained by direct integration. The second line lists adjusted parameters to correct the next-nearest contacts. The radius of the vdW distinct element is 2.71 nm.

ϵT (meV)	A	B	α	β
97.45	0.0104	1.31	9.5	3.5
71.24	0.0223	1.31	9.5	4

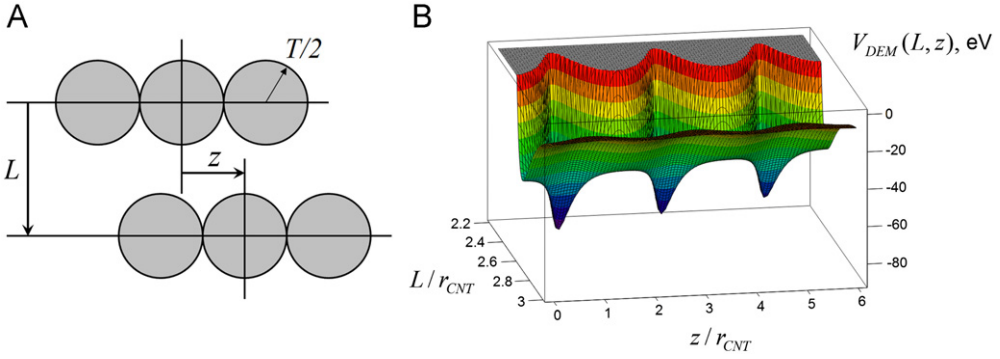

Fig. 5. (A) Intertube coordinate system. For an easier visualization, the radius of each spherical element was chosen $T/2$. (B) Surface plot of the interaction potential of two parallel finite (10,10) CNTs as a function of normalized intertube distance L and normalized misalignment z. For this example, $r_{CNT}=T/2$.

3.2.1. Interaction between parallel REs

In this subsection we focus only on the interaction of two parallel nanotubes. To restore the smoothness of the interaction we propose to introduce axial anisotropy of the contact model, which now takes a functional form depending on both the center to center distance R between the spherical elements and the misalignment angle θ, Fig. 6(A).

We adjust the axial dependence of the potential using Fourier series with fitted coefficients to counter the energetic preference for staggered orientation. After the adjustment, expression $V(R)$ of the vdW contact model remains unchanged, but the normalized distance D takes the form

$$D^k(R,\theta) = \frac{R}{r_{CNT}\Theta^k(\theta)} - 2. \tag{12}$$

The angular function $\Theta_k(\theta)$ of the order k writes

$$\Theta^k(\theta) = 1 + \sum_{i=1}^{k} C_i[(-1)^{i-1} + \cos(2i\theta)]. \tag{13}$$

We will refer to the contact model $V(R)$ with the adjustments (12) and (13) as $V^k(R,\theta)$. We label the resulted DEM intertube potential as $V^k_{DEM}(R,z)$. The set of k constants C_i can be determined via nonlinear fitting, by requiring equal values of the intertube potential for $k+1$ misaligned states evaluated at the equilibrium intertube distance L_0

$$V^k_{DEM}(L_0, z_i = iT/2k) = V^k_{DEM}(L_0, 0), \quad i = 1,..,k. \tag{14}$$

Note that the expression (13) is equal to 1 for $\theta = \pi/2$. However, because the next-nearest contacts are altered by the angular adjustment, the resulting intertube potential V^k_{DEM} will be affected even in the case of aligned CNTs ($z=0$). Therefore, the obtained potential should be renormalized so that it would give the correct value of adhesion energy for aligned configuration. This can be easily achieved by rescaling ϵ to an appropriate $K\epsilon$ value.

The parametrization of anisotropic adjustment of vdW contact model for (10,10) CNT is given in Table 3 below (the correction function used 3 harmonics). The resulting interaction between two (10,10) CNTs with aspect ratio of 15 is shown in Fig. 6(B). Our procedure of the potential "ironing" appears to be very effective. As one can see from the comparison of Figs. 5(B) and 6(B), the corrected pair potential gives more realistic potential, with suppressed periodic structure associated with spherical elements. Fig. 7(A) gives a polar plot of the obtained $\Theta^3(\theta)$ from which it becomes apparent that the potential V^3_{DEM} flattening via angular adjustment is due to shrinking of the real distance between misaligned REs ($\theta \neq \pi/2$). We emphasize once more that all these adjustments do not affect the intertube interaction of the perfectly aligned CNTs. This can be seen in Fig. 7(B), which compares $V^3(L,0)$ with the intertube potential obtained by the microscopic integration.

3.2.2. Interaction between crossed REs

Having solved the problem of formation of deep potential wells, we now focus on the case when two CNTs are crossed, with a crossing angle γ. This extension is done in such a way, that the crossing angle γ and anisotropy correction angle θ are orthogonal coordinates. One possible solution is to use the concept of "neutral" plane (Fig. 8). Within this approach the

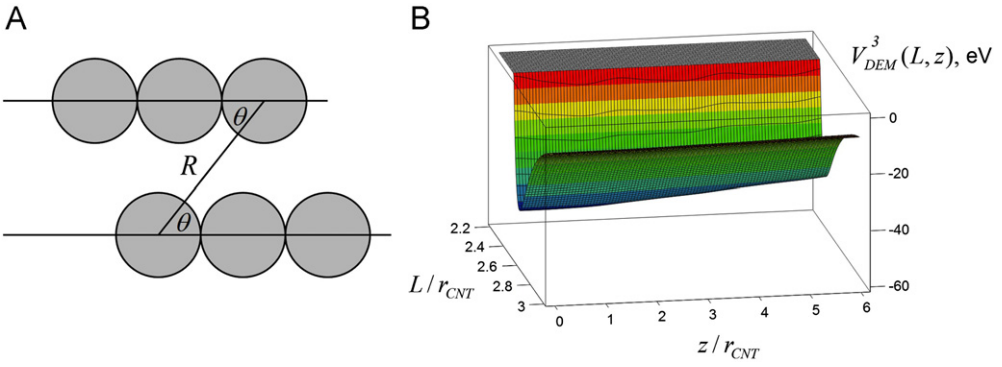

Fig. 6. (A) Polar coordinate system associated with pairs of spherical elements located on parallel CNTs. (B) Surface plot of the corrected intertube potential for the interaction of two parallel and finite (10,10) CNTs.

Table 3
Parametrization of anisotropic adjustments of the vdW contact between two (10,10) CNTs.

C_1	C_2	C_3	K	C_γ	δ
0.3440	0.0270	−0.0015	0.524	90	−7.5

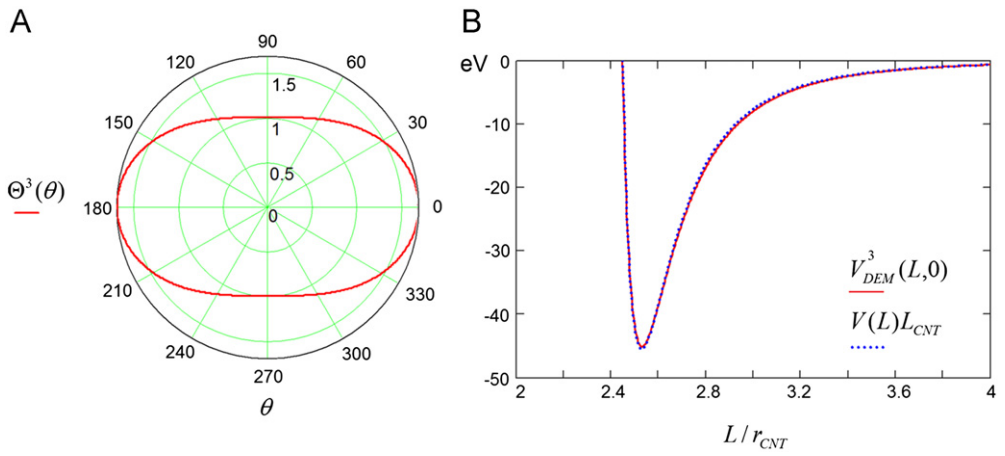

Fig. 7. Details on the anisotropic vdW contact model for (10,10) CNTs. (A) Polar plot of $\Theta^3(\theta)$. $\theta=\pi/2$ corresponds to face-to-face interaction between REs. (B) Corrected total potential as a function of normalized intertube spacing in comparison with the analytical intertube potential, multiplied by the length of the CNT.

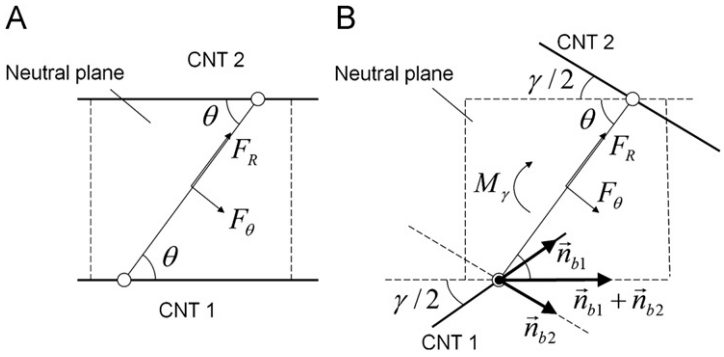

Fig. 8. The definition of angle variables (θ and γ) for the case of two (A) parallel and (B) crossed CNTs. The empty circles mark the centers of spherical particles.

angle θ in the case of crossed CNTs is defined as an angle between the contact unit vector $\vec{n}_R$ (directed from element 1 to element 2) and vector sum of first ($\vec{n}_{b1}$) and second ($\vec{n}_{b2}$) axial directions. This definition incorporates the limit case of parallel nanotubes and preserves kinematical independence between θ and the crossing angle γ, which allows to treat them as independent variables. The normal (F_R) and shear (F_θ) contact forces lay in uniquely defined "neutral" plane, which does not depend on permutation of first and second CNTs. An aligning moment (M_γ), acting between two misaligned CNT segments may be introduced as discussed below.

3.2.3. *Aligning moments*

The integrated LJ potential of two cylindrical segments depends on the angle γ between their axes. This leads to the presence of contact moments, that tend to align cylindrical segments. In the case of aspect ratios of the segments close to 1, angular dependence of the potential can be neglected, what is typically done in BS models. However, correct aligning moments are important for self-assembly processes. If we would like to consider an anisotropic nature of vdW interaction, that is predicted by macroscopic theories (Rajter et al., 2007), it is important to have the technical possibility of incorporation of the aligning moments. In this case the potential given by expressions (10), (12), and (13) has to be enriched with an additional multiplier, that favors certain orientations:

$$U(R,\theta,\gamma)=V^k(R,\theta)\Gamma(R,\gamma). \tag{15}$$

Similar to adjustment ((12) and (13)), such multiplier may be obtained as a Fourier series with respect to the angle γ. We find that anisotropy of the numerically integrated potential of two interacting cylinders is well described by a single harmonic adjustment

$$\Gamma(R,\gamma)=1+W_\gamma(R)(1-\cos(2\gamma)). \tag{16}$$

Here, the function $W_\gamma(R)$ determines the strength of anisotropy and the correct power of its decay with distance. Note that $\Gamma(R,\gamma)\le 1$, ($\Gamma(R,0)=1$).

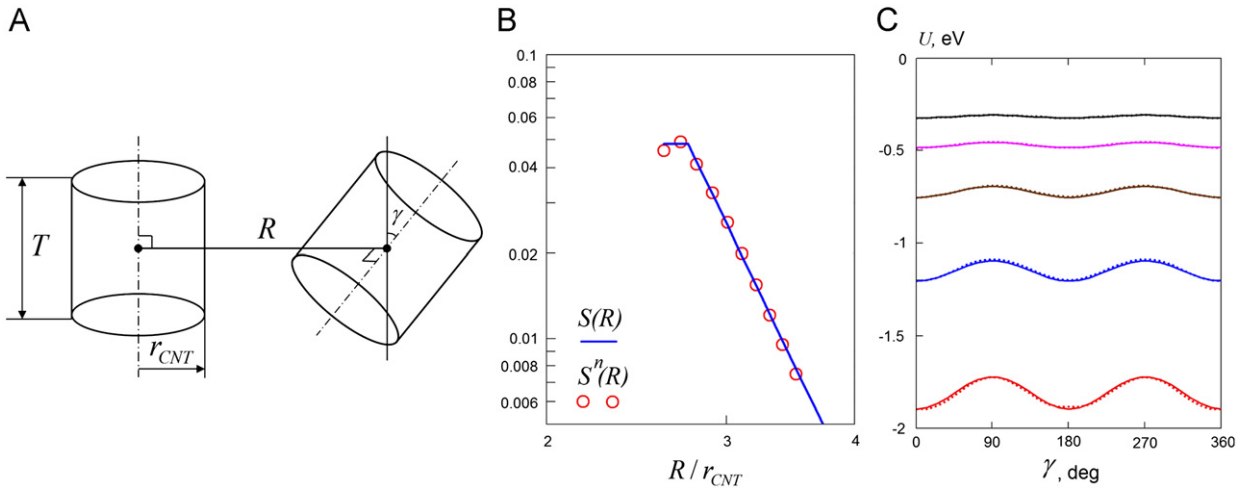

Fig. 9. (A) The geometry of the crossed cylindrical segments. (B) Numerically integrated anisotropy function $S^n(R)$, fitted with analytical expression (17). (C) Numerically integrated potential of interaction as the function of the crossing angle γ for few separation distances R (solid line) as compared to the analytical potential described by expressions (15)–(17).

Consider the approximation of anisotropy of LJ potential U^n, numerically integrated over the cylindrical segments with $T=2r_{CNT}$ (Fig. 9(A)). We assume that

$$W_\gamma(R)=C_\gamma(R/r_{CNT})^\delta. \tag{17}$$

We introduce the anisotropy function of the potential U as

$$S(R)=\frac{1}{2}\left|\frac{U(R,\theta,\gamma=0)-U(R,\theta,\gamma=\pi/2)}{U(R,\theta,\gamma=0)}\right| \tag{18}$$

and the same function for numerically integrated potential

$$S^n(R)=\frac{1}{2}\left|\frac{U^n(R,\gamma=0)-U^n(R,\gamma=\pi/2)}{U^n(R,\gamma=0)}\right|. \tag{19}$$

In the case of the potential given by expressions (10), (12), and (13)) with the adjustment (15)–(17) we have $S(R)=W_\gamma(R)$. In the case of numerically integrated potential this function can be found directly. We assume that it depends only on the intercenter distance R. Fig. 9(B) gives the numerical solution for $S^n(R)$ for few different distances R, presented in logarithmic coordinates. The numerical solution is fitted with the function $C_\gamma(R/r)^\delta$. The parameters C_γ and δ found by numerical fitting are given in Table 3.

Fig. 9(C) presents the comparison between analytical potential (15) and numerically integrated one, given as functions of the crossing angle γ for selected values of normalized separation distances R/r_{CNT}. It is observed that the analytical expressions (15)–(17) provide good representation of the angular dependence of the potential of two aligned ($\theta=\pi/2$) cylinders.

For the values of R smaller than $R_m=2.75r_{CNT}$ we assume that the anisotropy function is constant and equal to $S(R_m)=W(R_m)$. It is important to note that our adjustment (15)–(17) captures the angular dependence of the potential only for the attractive part of the potential, which is of practical importance for self-assembly problems. We do not consider the dependence associated with the repulsive part ($2r_{CNT}<R<R_m$), which may favor misaligned states.

3.2.4. *Corrected potential and the final vdW contact model*

Summarizing the previous subsections, we can write down the vdW contact of spherical elements as

$$U(R,\theta,\gamma)=f_c(R)V^k(R,\theta)\Gamma(R,\gamma), \tag{20}$$

$$V^k(R,\theta)=4K\epsilon\left(\frac{A}{(D^k(R,\theta))^\alpha}-\frac{B}{(D^k(R,\theta))^\beta}\right), \tag{21}$$

$$D^k(R,\theta)=\frac{R}{r_{CNT}\Theta^k(\theta)}-2, \tag{22}$$

$$\Gamma(R,\gamma)=1+W_\gamma(R)(1-\cos(2\gamma)), \tag{23}$$

$$\Theta^k(\theta) = 1 + \sum_{i=1}^{k} C_i((-1)^{i-1} + \cos(2i\theta)), \tag{24}$$

$$W_\gamma(R) = C_\gamma (R/r_{CNT})^\delta. \tag{25}$$

The parameters for vdW contact model are presented in Tables 2 and 3; the smooth cutoff function $f_c(R)$ is given in the Appendix. Normal force, shear force and aligning moment acting between two distinct elements can be found as

$$F_R = -\frac{\partial U}{\partial R}, \quad F_\theta = -\frac{1}{R}\frac{\partial U}{\partial \theta}, \quad M_\gamma = -\frac{\partial U}{\partial \gamma}. \tag{26}$$

The corresponding stiffness are

$$k_R = \left|\frac{\partial^2 U}{\partial R^2}\right|, \quad k_\theta = \left|\frac{1}{R^2}\frac{\partial^2 U}{\partial \theta^2}\right|, \quad k_\gamma = \left|\frac{1}{R^2}\frac{\partial^2 U}{\partial \gamma^2}\right|. \tag{27}$$

4. Mesoscopic DEM simulations of CNTs

We now demonstrate the suitability of the created model to investigate the mechanics of a wide range of (10,10) CNT systems, including CNT films.

4.1. Adhesive shear strength and viscous friction of CNT sliding

In this example we demonstrate the importance of the created anisotropic vdW contact model. We consider the adhesive shear strength and viscous friction coefficient of two CNTs. These parameters are important for estimation of the macroscopic mechanical properties of CNT-based materials. The simulation setup for determining adhesive shear strength is as follows: two (10,10) CNTs of the same length $L_{CNT} = 40.7$ nm originally are parallel and aligned, with intercenter distance L_0 (Fig. 10(A)).

In one set of simulations, CNT 1 is fixed at one of its ends, and CNT 2 is pulled in a force controlled mode. We can measure the adhesive shear strength as a minimum force F_0 sufficient to fully separate CNT 2 from CNT 1. The simulation has been performed for the model of vdW interactions based on both the simple isotropic contact model and for the anisotropic model described in Sections 3.1 and 3.2, respectively. The results of both simulations are summarized in Table 4. As a reference, the line before last in Table 4 indicates the lowest possible value ζ, which is the cohesive energy per unit length predicted analytically with the potential (10) $\zeta = V(L_0)/T$. Note that ζ does not depend on L_{CNT}.

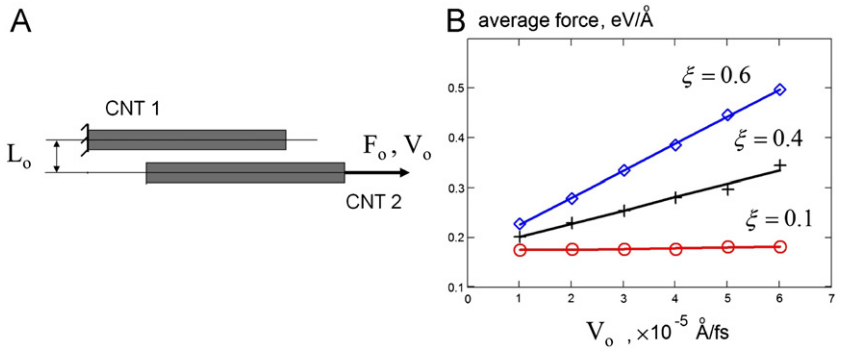

Fig. 10. (A) Adhesive shear strength and viscous friction coefficient measurement—schematics of the DEM simulation setup. (B) Averaged forces measured in displacement control DEM sliding simulations as functions of velocities for three different damping coefficients.

Table 4
Adhesive shear strength between two parallel CNTs for different intertube vdW contact models. The last line is based on the work of Filleter et al. (2012) and refers to (27,0) CNTs.

V	F_0 (eV/Å)	F_0/L_{CNT} (eV/Å^2)	F_0/L_{CNT} (pN/Å)
V_{DEM}	8.590	0.021	33.85
V^3_{DEM}	0.295	7.25×10^{-4}	1.16
ζ	0.224	5.51×10^{-4}	0.88
MD	0.19 ± 0.06	$(4.57 \pm 1.52) \times 10^{-4}$	0.73 ± 0.25

On one hand, simulations using the isotropic contact gives high adhesive strength, which is typical for pair potential models. The value obtained here of 33.85 pN/Å qualitatively agrees with the previously reported value of 26.86 pN/Å for (5,5) CNTs (Buehler, 2006) obtained from BS simulation with Lennard-Jones pair potential between beads. On the other hand, the adhesive shear strength predicted by the model with anisotropic vdW contact is 1.16 pN/Å. This is close to the lowest bound limit, of 0.88 pN/Å, and the MD obtained value of approximately 0.73 pN/Å (Filleter et al., 2012).

A second set of simulations were performed in a displacement controlled mode, when the CNT 2 is pulled horizontally with a prescribed velocity v_0. The results of such a test (Fig. 10(B)) utilizing the anisotropic vdW contact obtains that within a certain range of velocities, the average force acting on the edge element depends linearly on speed. Fig. 10(B) allows us to estimate viscous friction coefficient: for $\xi = 0.4$ (see Section 2), which is used in further simulations, it is equal to 4.3×10^{-5} μN s/m. This value is orders of magnitude smaller than the 10 μN s/m realistic value used with the isotropic vdW model (Cranford and Buehler, 2010). We recall that ξ was introduced to solve the technical difficulties associated with the numerical integration of the equations of motion (1). As the viscous behavior depends on ξ, this example points out that care must be exercised in simulations in which the dynamic aspect of CNTs sliding against each other is dominant. Also, it points out the need to account for the realistic viscous behavior.

Note that in the limit of zero velocity Fig. 10(B) gives the value of force sufficient to overcome the static friction and start the CNT sliding motion. Due to topology of the vdW potential this value does not coincide with the value of force needed to fully separate the two CNTs, which is approximately 1.5 times larger.

4.2. CNT ring self-assembly and stability

In this example we demonstrate the importance of both the created anisotropic vdW contact model and the DEM ability to simulate a self-assembly processes. Unclosed CNT rings are often encountered in experiments involving isolated CNTs (Martel et al., 1999). The CNT ring formation was previously considered in Anderson et al. (2010) using the isotropic vdW contact model, based on pair potential (10). Reasonable smoothness of the intertube interaction was achieved there by choosing very small ratio of T/r_{CNT}, i.e. a much finer coarse-grading than the one exemplified here in Section 2. This has lead to a computational time of about 2 h on a standard laptop. Here, based on an anisotropic contact model, the numerical solution of the same problem was obtained in approximately 1 min. The (10,10) CNT of length $L_{CNT} = 271.2$ nm was represented by 200 elements. The initial and final configuration of the CNT ring given in Fig. 11(A) demonstrates that the method is able to handle large displacements caused by the vdW forces, a feature which will be important for simulating processes by which CNT films develop bundles. The simulation of the relaxation required 24,000 time steps or 0.6 ns. Fig. 11(B) shows the evolution of the different energy terms. As can be seen from the plots, the final equilibrium state is characterized by the balance of elastic strain energy and vdW potential energy.

From the continuum perspective, the equilibrium parameters of a CNT ring can be predicted with the simple analytical model described next. Consider the ring shown in Fig. 11(C), with radius R_r, length L_{CNT}, and overlap length Δl. We assume

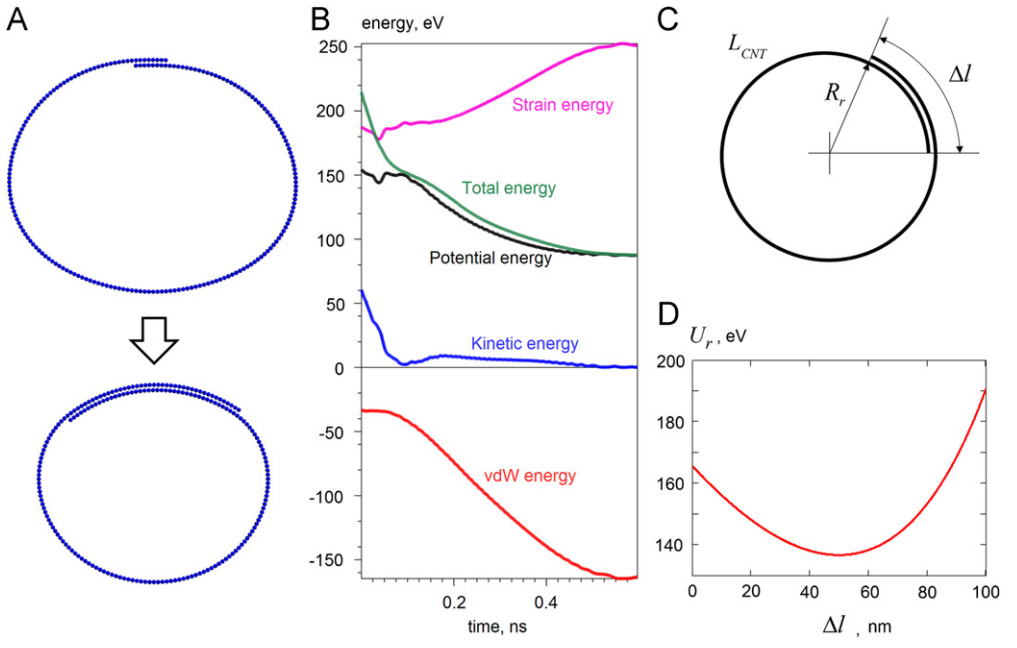

Fig. 11. CNT ring relaxation. (A) Evolution of the CNT ring shape during the DEM simulation. (B) Evolution of energy terms during the simulation. (C) Schematics for the simplified analytical model. (D) Potential energy as a function of the overlap segment length for the analytical model.

for simplicity the ideal circular shape of an equilibrium ring configuration. The vdW adhesion energy of a ring with overlap Δl may be well approximated as $-\zeta\Delta l$. Assume also that the strain energy of a deformed CNT is the energy of an elastic beam in pure bending state under the bending moment M

$$U_{str}=\frac{M^2}{2YI_c}L_{CNT}=\left(\frac{YI_c}{R_r}\right)^2\frac{L_{CNT}}{2YI_c}=\frac{YI_cL_{CNT}}{2R_r^2}=\frac{YI_cL_{CNT}}{2}\frac{4\pi^2}{(L_{CNT}-\Delta l)^2}. \tag{28}$$

Here I_c is a moment of inertia of a hollow circular cross section. The total potential energy of the ring (Fig. 11(D))

$$U_r=-\zeta\Delta l+\frac{2\pi^2YI_cL_{CNT}}{(L_{CNT}-\Delta l)^2} \tag{29}$$

has a minimum for

$$\Delta l=L_{CNT}-\sqrt[3]{\frac{4\pi^2YI_cL_{CNT}}{\zeta}}. \tag{30}$$

The equilibrium configuration reached by the DEM simulation in the "hands off" manner is characterized by $\Delta l=51.5$ nm, which is in close agreement with the $\Delta l=49.7$ nm value assessed with Eq. (30).

To gain a microscopic perspective, we also investigated how the CNT ring morphology obtained by DEM compares with the one obtained by direct MD simulations. The same (10,10) CNT ring was simulated using the MD code Trocadero (Rurali and Hernandez, 2003) using a classical Tersoff (1988) potential to describe the covalent bonding between carbon atoms, and a microscopic LJ potential with the parameters given in Section 2 to capture the long-ranged bonding. We started the microscopic simulations from a circular ring state with the equilibrium overlap distance predicted by the mesoscopic model. The system containing 132,900 atomic degrees of freedom was evolved in time from a "cold" start for 7.4 ps with a velocity Verlet algorithm. The atomistic simulations demonstrated good agreement in the most important details. During the MD simulation time, the overlap length and the ring radius did not change significantly (Fig. 12(A)). Due to the increase in stiffness at the overlap, the ring lost its perfect circular shape, a feature observed also with DEM. There are however certain details, such as the "buckling" of the CNT surface at the point of contact with the inner CNT end (Fig. 12(B)), and the small separation of the outer end (Fig. 12(C)), that were not captured by the DEM mesoscopic model. The buckling visible in Fig. 12(B) is the signature of the long range vdW interaction. It cannot be attributed to the known nonlinear elastic buckling of the CNT in pure bending because the curvature reached in this simulation is small (Nikiforov et al., 2010.). The equilibrium ring radius in our simulations is 34.9 nm, which is larger than the critical radius for buckling of 27.5 nm (Volkov and Zhigilei, 2010c).

It is worth to note that the microscopic simulation took 150 h on one core of a computational cluster, which is approximately 2×10^5 times slower than the DEM simulation for the whole ring formation.

4.3. Twisting of a CNT nanorope

This example illustrates the importance of accounting in the mesoscopic model for both moments and forces acting on the spherical particles. We recall from Section 2 that restoring moments are developed in the parallel bonds in response to relative angular displacements between spherical particles. Because in the DEM in mesoscopic model the spherical particles are treated as rigid bodies, torsional deformations can be simulated in individual CNTs. Torsional degrees of freedom in CNT systems present importance for applications of engineering significance. For example, twisting has been applied in order to improve mechanical properties of CNT ropes (Zhang et al., 2007).

Consider a nanorope, consisting of 37 (10,10) CNTs, each of length 67.8 nm. Individual CNTs in the nanorope were placed in a honeycomb arrangement, with distances between CNTs equal to L_0. At the initial moment of the simulation all

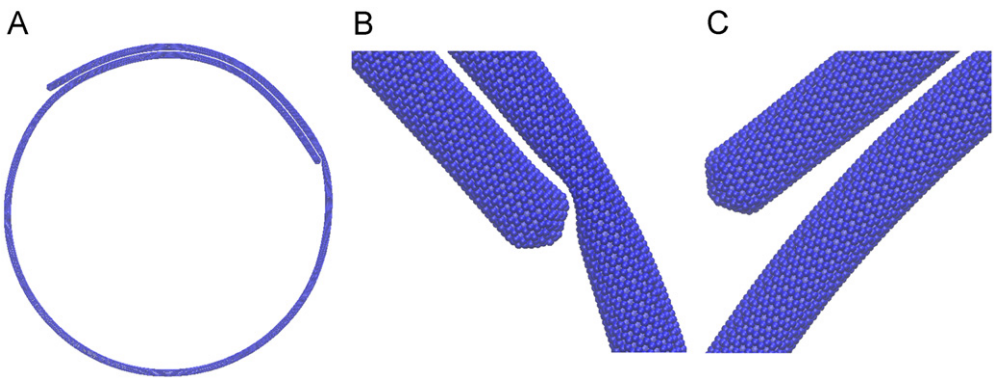

Fig. 12. Molecular dynamic simulation of a (10,10) CNT ring. (A) Ring shape after 7.4 ps of time evolution. (B) Buckling of a CNT at the point of contact with its edge. (C) Separation of the free edge of a CNT. Visualization was carried out using VMD (Humphrey et al., 1996).

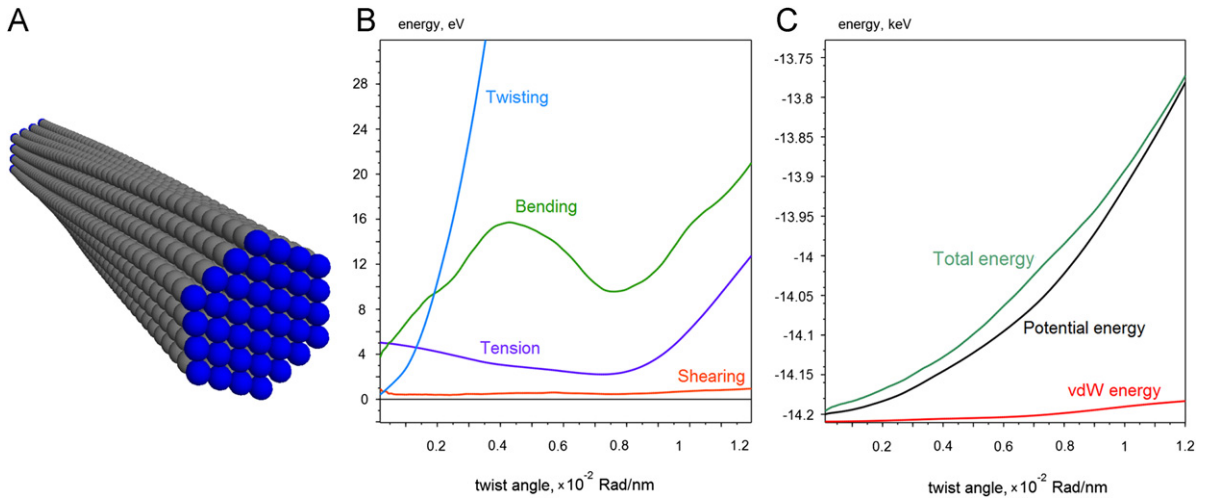

Fig. 13. (A) DEM simulations of a twisted nanorope (free elements in gray, grip elements in blue) composed of (10,10) CNTs. (B) Evolution of different elastic energy terms. (C) Total energy, potential energy and vdW energy. (For interpretation of the references to color in this figure caption, the reader is referred to the web version of this article.)

CNTs are undeformed. Both translational and rotational degrees of freedom of the edge elements of the nanorope are rigidly fixed with respect to the grips that are rotating in opposite directions at a prescribed rate of 1.15 deg/ps. Fig. 13(A) gives the deformed configuration of the nanorope. The strain energy in such a test involves twisting, shearing, tension and bending mode contributions. However, as can be seen from Fig. 13(B), for relatively large twisting angles the response is clearly dominated by twisting of individual CNTs. The torsional stiffness of the rope is 1.312 keV, which is approximately equal to the torsional stiffness of 37 individual tubes. An interesting question arises from the problem of a twisted nanorope—is there an intrinsic twist at the equilibrium state of free nanorope (Liang and Upmanyu, 2005)? The DEM simulations obtained that the minimum of potential energy of the nanorope corresponds to undeformed configuration (Fig. 13(C)), i.e. a stress-free nanorope composed of armchair CNTs does not self-twist.

4.4. *Self-assembly of a randomly oriented network of nanotubes*

The numerical modeling of the complex self-assembly processes present in CNT papers represent a challenging test for our model. Predicting the microstructure of the CNT-based material (paper) is a matter of capturing the correct aligning moments between CNTs, adhesive shear strength, and interaction cutoff radius. Agreement with experiment on important features, like CNTs mobility leading to bundles formation, Fig. 1, would represent an important validation for our mesoscopic model.

The remarkable qualitative agreement with experiment and microscopic simulations obtained in the examples considered in the previous subsections, is a credible basis for simulating the more complex self-assembly process of CNT papers. We considered 150 (10,10) CNTs each of 0.2 μm in length. Initially straight CNTs are located in a box volume, which can be viewed as a piece of CNT paper. The CNT centers are chosen randomly in $300 \times 300 \times 20$ nm^3 cuboid. CNT orientations are distributed isotropically in the CNT paper plane, with uniformly distributed random out-of-plane angle within the borders of 10°. In the case of overlap of CNT segments the contact forces (26) are artificially replaced with constant normal repulsive force of 1 eV/Å. The resulting specimen has the porosity of about 87% (we define zero porosity as the porosity of closely packed parallel CNTs).

On one hand, simulations carried out with a vdW model based on the pairwise potential (10) obtained that the CNTs do not tend to form bundles (Fig. 14(A)). Due to high adhesive shear strength CNTs showed low mobility; most of tubes remained where they were deposited; some neighboring tubes formed bundles of 2–3 CNT. Fig. 14(B) gives the evolution of the energy terms during this simulation. During the 0.5 ns (22,000 time steps) the kinetic energy of the system dropped to zero while the variations of other energy terms almost stopped.

On the other hand, the simulation based on our anisotropic vdW contact model indeed has demonstrated qualitatively different behavior. Fig. 14(D) shows the final configuration for a set of CNTs evolved in time using the potential (20). The simulation took 2×10^5 time steps (4.5 ns) and about 100 hours on a regular desktop machine. The self-assembly process was characterized by much higher mobility, and CNTs showed the tendency to unite into bigger bundles even after 4 ns. Almost all CNTs were joined into bundles comprising from 2 to 25 individual CNTs. Nanotubes within each bundle were untwisted and displayed honeycomb hexagonal alignment (see inset in Fig. 14(D)). These facts are in qualitative agreement with the structure of CNT paper observed in electron microscopy, as well as the results of MFF simulations (Volkov et al., 2008; Volkov and Zhigilei, 2010a–c). No CNT rings were formed during the simulation time, indicating that this self-folding mode might be a feature of isolated CNTs.

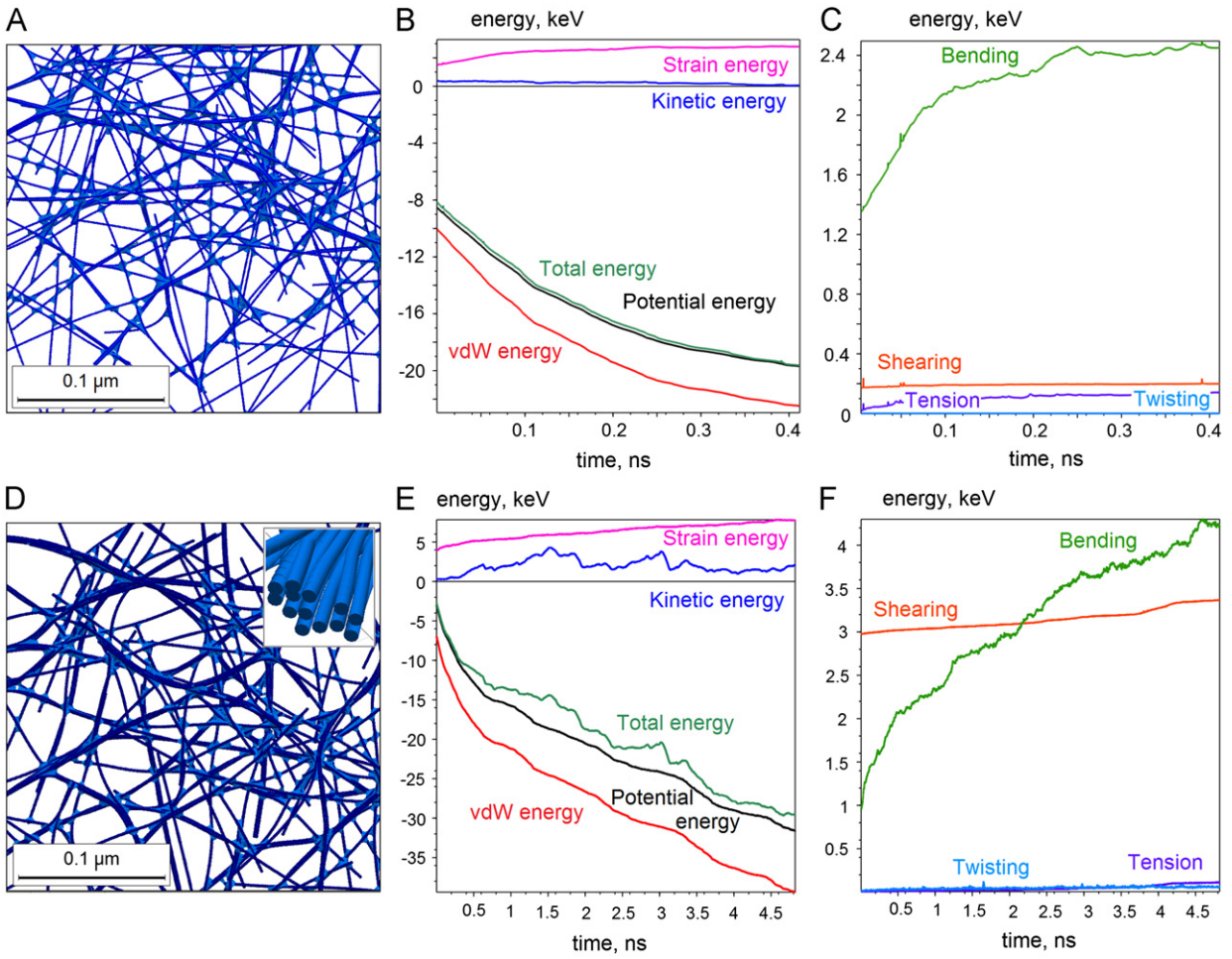

Fig. 14. CNT paper structure (A,D), evolution of different energy terms (B,E), evolution of elastic energy terms (C,F) in the simulation based on isotropic (A–C) and anisotropic (D–F) contact models.

Fig. 14(E,F) shows an evolution of different terms of potential energy, as well as kinetic and total energy of the system during the simulation. (The initial part of relaxation, characterized by large changes in energies was excluded from these plots.) An important feature is the relatively large kinetic energy present during the simulation, indicating a high mobility of sliding CNTs. It is seen that during the simulation time, the system did not reach an equilibrium state. However, the strain and vdW energy curves in Fig. 14(E) suggest that eventually there should be an equilibrium state arising from the balance of elastic energy and vdW energy, just like in the CNT ring example from the previous subsection. Fig. 14(F) shows the relationship between different terms of elastic energy during the simulation. An interesting feature is the relatively large elastic energy stored by the parallel bonds in shearing, whereas normal stretching is almost absent. This behavior contrasts with the one obtained with the isotropic contact model, in which most elastic energy is stored in the bending deformation (Fig. 15(C)) of individual CNTs.

The above comparison indicates that the two most important parameters that affect the stability of the structure are the adhesive shear strength between parallel CNTs and the aligning moment between the crossed CNTs. Thus, the effort to include these two features in our mesoscopic model is fully justified. Clearly, mesoscopic models employing vdW pair potentials (Anderson et al., 2010; Buehler, 2006) are less suited for such endeavor mainly because of the staggering effect discussed in Section 3. Recent work indicated that some other factors, such as CNTs nonlinear elastic buckling (not accounted here) may be of importance (Volkov and Zhigilei, 2010a–c). It is also important to note that the "hands-off" bundling process is influenced by other parameters, such as the initial porosity. In case of a very porous initial state, CNTs do not form bundles (even with the anisotropic vdW model) because of insufficient number of CNTs forming vdW contacts. In very dense random specimens the high initial entanglement prevents large CNTs rearrangements at least during the affordable computational time. Interestingly, our self-assembly simulations suggest that there is an optimal density of a random carbon nanotube sample that leads to the formation of relatively large CNT bundles.

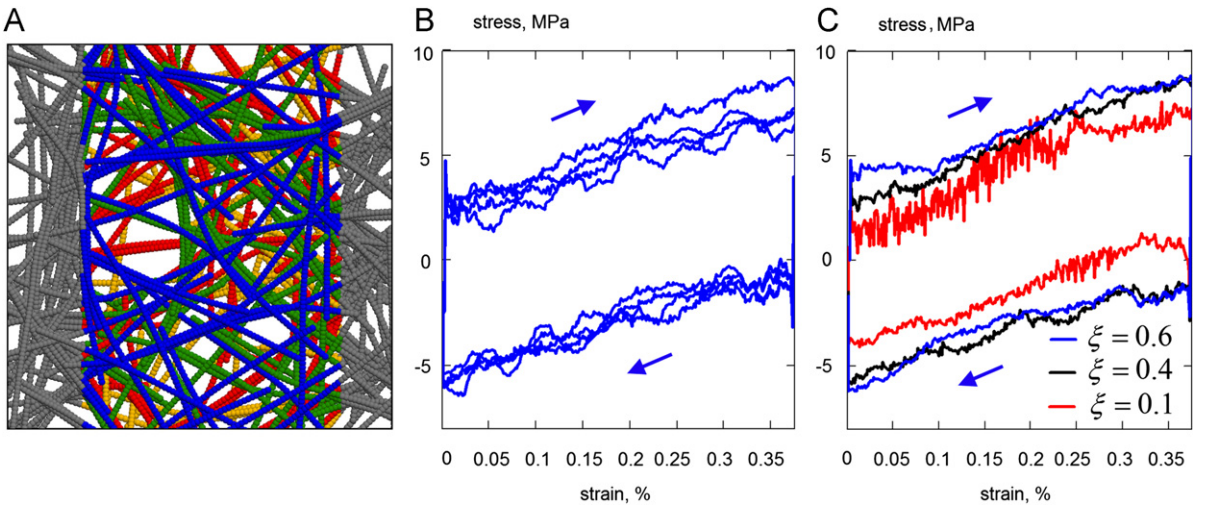

Fig. 15. Mechanical test on CNT film specimen. (A) Multilayered CNT film. Different colors are used to indicate different layers. Grip elements are in gray. (B) Four loading–unloading cycles of a constant rate tension-compression test, that show viscoelastic response of the specimen. (C) Three loading–unloading cycles of a constant rate tension-compression test but different ξ. (For interpretation of the references to color in this figure caption, the reader is referred to the web version of this article.)

4.5. Tensile test on a low porosity CNT paper specimen

A common experimentally relevant mechanical test is the tensile deformation of a CNT paper. The DEM simulation of this process is discussed next. The method described in previous subsection allows the preparation of a CNT paper specimen. Unfortunately, that approach is applicable only for porous specimens. The results of mechanical tests on such specimens are non representative due to high heterogeneity of the paper structure. As already mentioned, attempts to produce specimens with low porosity proved to be computationally prohibitive. In order to assembly a denser specimen, a "layer by layer" assembly procedure is instead employed. This procedure is as follows: the CNTs of the current layer are placed into the cuboid volume and relaxed for 0.4 ns. The tubes of each next layer are placed in the neighboring volume, and allowed to relax and deposit on the previous layer. Such procedure reflects the physics behind the assembly of CNTs into a paper using the filtration process. The resulting specimen shown in Fig. 15(A) consists of four layers, has the porosity of about 68% and qualitatively realistic structure. It contains 240 (10,10) CNTs, where the length of each CNT is 95 nm.

Next, the relaxed specimen is subjected to a few loading cycles of a displacement controlled tension-compression test. The distinct elements of the specimen are separated into three groups: two "grips" and free elements. The elements of grips are moved with the constant speed of 5 m/s in opposite directions, whereas other degrees of freedom of the grip elements are free. The test consists of loading and unloading, each take 3000 time steps or 0.04 ns.

Viscoelastic behavior of a CNT films and composites is commonly observed in mechanical experiments (Suhr et al., 2005). In our simulated test, the specimen demonstrates linear viscoelastic behavior in a narrow range of strains. The obtained loading–unloading hysteresis loop (Fig. 15(B)) is well described by a simple parallel linear spring–damper Kelvin–Voigt model (see for example Bulicek et al., 2012) with Young's modulus and viscosity constants of 1.9 GPa and 0.06 Pa s, respectively. Results on the repeatability of such tensile tests (not shown) indicated that the variation of mechanical parameters of the specimens are within the reasonable range of 20%.

We also carried out similar simulations of loading–unloading cycles for various ξ parameters, in order to investigate the role of local damping. The results displayed in Fig. 15(C) indicate that the slope and the vertical width of the loop (vertical distance between loading-unloading cycle measuring the viscosity of the material) are not dominated by the numerical parameter ξ. This behavior contrasts with the one noted in Section 4.1. Physically, this is because the response obtained here is mainly due to the covalent forces of individual CNTs, and not by the rate-dependent sliding shear forces. Overall, this example demonstrates that the existing numerical approach of integrating the equations of motion using the artificial local damping approach is still useful.

5. Summary

Building on our recent proposal (Anderson et al., 2010), in this paper we demonstrate that DEM, a methodology designed for large-scale engineering problems, can be successfully adapted at the mesoscale and used to bridge the gap between the large spatial scales exhibited by the mechanical phenomena that we desire to simulate and the interatomic forces that limit the current high-resolution microscopic methods. Starting from an atomistic description of CNTs, we grouped atoms into spherical particles that interact with each other via prescribed contact models encapsulating the vdW and covalent interatomic

interactions. An important feature is the presented anisotropic vdW contact model that resolves the problems of high adhesive shear strength and low aligning moments associated with the isotropic LJ treatments of the vdW interaction between coarse grained elements. The promising potential of the DEM methodology to simulate complicated and demanding phenomena of CNT self-assembly and mechanical response of CNT papers was illustrated with several examples.

All the presented examples involved a created mesoscopic model for a (10,10) CNTs in which each spherical particle lumps about 220 carbon atoms. A more significant reduction in atomistic degrees of freedom, achieved for example by the coupling of the method with continuum-level modeling such as finite element, can make the methodology even more efficient. Nevertheless, to model other complex phenomena, such as yielding and fracture (Dumitrică et al., 2003, 2006), the model needs to be also expanded in the microscopic region, by replacing separate coarse-grained beads with full atomistic models in the highly stressed regions.

The basic DEM model introduced here can be further expanded for atomistically informed hierarchical multiscale modeling of a variety of processes and applications. For example, in mechanical energy storage applications CNTs are severely deformed. Recent simulations (Huang et al., 2008; Nikiforov et al., 2010; Zhang et al., 2009) indicated that the onset of the nonlinear behavior (rippling and buckling) in CNTs under bending and twist deformations leads to a reduction in the elastic constants. This change in elastic constants can be easily incorporated in the current parallel bond contact model, used here to capture only the CNT linear elasticity. The fracture process of individual CNTs can be simplistically modeled by limiting the strength of the parallel bonds. This method development can be particularly useful in approaching the study of the strength of CNT ropes. More precisely, it could allow understanding the correlation between the well-documented high tensile strength of individual CNTs (Dumitrică et al., 2003, 2006) with that of the rope made from them, which can be twisted (Zhang et al., 2007). In nanocomposite material applications, CNTs are functionalized in order to improve the mechanical load transfer. CNT interactions beyond the vdW interactions, such as CNT linking (functionalization) via covalent bonds. If such bonds do not introduce significant rotational stiffness, their effects can be readily captured by adding into the current DEM model another type of standard DEM bonds called contact bonds (Itasca CG Inc., 2008). The contact bond (to be parameterized microscopically) behaves, essentially, as a parallel bond of radius zero. Thus, a contact bond cannot resist a bending moment or oppose rolling; rather, it can only resist a force acting at the contact point (Potyondy and Cundall, 2004).

Interesting prospects emerge due to the continuous development of DEM for performing complex engineering investigations. The DEM code that was used in the presented simulations, PFC3D 4.0, will be soon upgraded by the next version, PFC3D 5.0. The new code appears to be even better suited to performing mesoscopic simulations of CNTs, because it will support: (a) direct specification of a non-zero interaction radius for each spherical particle to ensure that a contact forms when these radii overlap, (b) modeling within a periodic space in which particles and contacts can migrate seamlessly across the periodic boundaries, and (c) automatic multi-threading to increase execution speed.

Acknowledgement

We are grateful to Henryk Stolarski and Erik Hobbie for helpful comments. We thank Itasca Education Partnership Program, NSF CAREER under Grant no. CMMI-0747684, and NSF under Grant no. CMMi 0800896.

Appendix A. The contact model for vdW interaction of two cylindrical segments

All simulations described in this paper were performed using the PFC3D 4.0 code (Itasca CG Inc., 2008). It was originally oriented on modeling large assemblies of rigid spherical particles, or rigid clumps of spherical particles. Here we consider the introduction of an anisotropic contact model of vdW interactions.

The axial direction of the nanotube, that determines anisotropy, is calculated for each ball as a vector, connecting the centers of its left and right neighbors (for each edge ball—as center-to-center vector between the ball and its only neighbor), and is stored in extra memory slots at each step of simulation for each ball. These data are used by the user-defined contact model (Itasca CG Inc., 2008), that is based on the potential (20).

Given normals $\vec{n}_{b1}$, $\vec{n}_{b2}$, $\vec{n}_R$ and distance R, the unit normal directions of shear force and aligning moment are found as

$$\vec{n}_\theta = \frac{\vec{n}_R \times [\vec{n}_R \times (\vec{n}_{b1} + \vec{n}_{b2})]}{|\vec{n}_R \times [\vec{n}_R \times (\vec{n}_{b1} + \vec{n}_{b2})]|}, \quad (\vec{n}_R \nparallel \vec{n}_{b1} + \vec{n}_{b2}),$$

$$\vec{n}_\gamma = \frac{\vec{n}_{b1} \times \vec{n}_{b2}}{|\vec{n}_{b1} \times \vec{n}_{b2}|}, \quad (\vec{n}_{b1} \nparallel \vec{n}_{b2}). \tag{31}$$

The user-defined PFC3D contact model requires to specify the potential, forces (moments) and stiffnesses. Potential is used to calculate global potential energy of the system. The expressions for forces and moments determine the dynamics of the system. The expressions for current stiffnesses are used by PFC3D to calculate the stable timestep (see Itasca CG Inc., 2008 for details), and viscous damping constants (if used).

Our contact model is given by the potential

$$U(R,\theta,\gamma) = \Gamma(R,\gamma) f_c(R) V^k(R,\theta). \tag{32}$$

The normal and shear forces and aligning moment are given by

$$F_R = -\frac{\partial U}{\partial R} = -\frac{\partial \Gamma(R,\gamma)}{\partial R} f_c(R) V^k(R,\theta) - \Gamma(R,\gamma)\frac{\partial f_c(R)}{\partial R} V^k(R,\theta) - \Gamma(R,\gamma) f_c(R)\frac{\partial V^k(R,\theta)}{\partial R},$$
$$F_\theta = -\frac{1}{R}\frac{\partial U}{\partial \theta} = -\frac{1}{R}\Gamma(R,\gamma) f_c(R)\frac{\partial V^k(R,\theta)}{\partial \theta},$$
$$M_\gamma = -\frac{\partial U}{\partial \gamma} = -\frac{\partial \Gamma(R,\gamma)}{\partial \gamma} f_c(R) V^k(R,\theta). \tag{33}$$

The corresponding stiffnesses are

$$\begin{aligned} k_R = \left|\frac{\partial^2 U}{\partial R^2}\right| = \Bigg| &\left(\frac{\partial^2 \Gamma(R,\gamma)}{\partial R^2} f_c(R) + \frac{\partial \Gamma(R,\gamma)}{\partial R}\frac{\partial f_c(R)}{\partial R}\right) V^k(R,\theta) + \frac{\partial \Gamma(R,\gamma)}{\partial R} f_c(R)\frac{\partial V^k(R,\theta)}{\partial R} \\ &+ \left(\frac{\partial \Gamma(R,\gamma)}{\partial R}\frac{\partial f_c(R)}{\partial R} + \Gamma(R,\gamma)\frac{\partial^2 f_c(R)}{\partial R^2}\right) V^k(R,\theta) + \Gamma(R,\gamma)\frac{\partial f_c(R)}{\partial R}\frac{\partial V^k(R,\theta)}{\partial R} \\ &+ \left(\frac{\partial \Gamma(R,\gamma)}{\partial R} f_c(R) + \Gamma(R,\gamma)\frac{\partial f_c(R)}{\partial R}\right)\frac{\partial V^k(R,\theta)}{\partial R} + \Gamma(R,\gamma) f_c(R)\frac{\partial^2 V^k(R,\theta)}{\partial R^2}\Bigg|, \end{aligned}$$
$$k_\theta = \left|\frac{1}{R^2}\frac{\partial^2 U}{\partial \theta^2}\right| = \left|\frac{1}{R^2}\Gamma(R,\gamma) f_c(R)\frac{\partial^2 V^k(R,\theta)}{\partial \theta^2}\right|,$$
$$k_\gamma = \left|\frac{1}{R^2}\frac{\partial^2 U}{\partial \gamma^2}\right| = \left|\frac{1}{R^2}\frac{\partial^2 \Gamma(R,\gamma)}{\partial \gamma^2} f_c(R) V^k(R,\theta)\right|. \tag{34}$$

Here

$$V^k(R,\theta) = 4K\epsilon\left(\frac{A}{(D^k(R,\theta))^\alpha} - \frac{B}{(D^k(R,\theta))^\beta}\right),$$
$$\frac{\partial V^k(R,\theta)}{\partial R} = 4K\epsilon\left(-\frac{\alpha A}{(D^k(R,\theta))^{\alpha+1}} + \frac{\beta B}{(D^k(R,\theta))^{\beta+1}}\right)\frac{\partial D^k(R,\theta)}{\partial R},$$
$$\frac{\partial V^k(R,\theta)}{\partial \theta} = 4K\epsilon\left(-\frac{\alpha A}{(D^k(R,\theta))^{\alpha+1}} + \frac{\beta B}{(D^k(R,\theta))^{\beta+1}}\right)\frac{\partial D^k(R,\theta)}{\partial \theta},$$
$$\frac{\partial^2 V^k(R,\theta)}{\partial R^2} = 4K\epsilon\left(\frac{\alpha(\alpha+1)A}{(D^k(R,\theta))^{\alpha+2}} - \frac{\beta(\beta+1)B}{(D^k(R,\theta))^{\beta+2}}\right)\frac{\partial D^k(R,\theta)}{\partial R} + 4K\epsilon\left(-\frac{\alpha A}{(D^k(R,\theta))^{\alpha+1}} + \frac{\beta B}{(D^k(R,\theta))^{\beta+1}}\right)\frac{\partial^2 D^k(R,\theta)}{\partial^2 R}$$
$$\frac{\partial^2 V^k(R,\theta)}{\partial \theta^2} = 4K\epsilon\left(\frac{\alpha(\alpha+1)A}{(D^k(R,\theta))^{\alpha+2}} - \frac{\beta(\beta+1)B}{(D^k(R,\theta))^{\beta+2}}\right)\frac{\partial D^k(R,\theta)}{\partial \theta} + 4K\epsilon\left(-\frac{\alpha A}{(D^k(R,\theta))^{\alpha+1}} + \frac{\beta B}{(D^k(R,\theta))^{\beta+1}}\right)\frac{\partial^2 D^k(R,\theta)}{\partial^2 \theta},$$
$$D^k(R,\theta) = \frac{R}{r_{CNT}\Theta^k(\theta)} - 2,$$
$$\frac{\partial D^k(R,\theta)}{\partial R} = \frac{1}{r_{CNT}\Theta^k(\theta)},$$
$$\frac{\partial D^k(R,\theta)}{\partial \theta} = -\frac{R\Theta^k(\theta)'_\theta}{r_{CNT}\Theta^k(\theta)^2},$$
$$\frac{\partial^2 D^k(R,\theta)}{\partial^2 R} = 0,$$
$$\frac{\partial^2 D^k(R,\theta)}{\partial^2 \theta} = -\frac{R}{r_{CNT}\Theta^k(\theta)^2}\frac{\partial^2 \Theta^k(\theta)}{\partial^2 \theta} + \frac{2R}{r_{CNT}\Theta^k(\theta)^3}\left(\frac{\partial \Theta^k(\theta)}{\partial \theta}\right)^2, \tag{35}$$

$$\Theta^k(\theta) = 1 + \sum_{i=1}^{k} C_i((-1)^{i-1} + \cos(2i\theta)),$$
$$\frac{d\Theta^k(\theta)}{d\theta} = -\sum_{i=1}^{k} 2iC_i \sin(2i\theta),$$
$$\frac{d^2\Theta^k(\theta)}{d\theta^2} = -\sum_{i=1}^{k} 4i^2 C_i \cos(2i\theta), \tag{36}$$

$$\Gamma(R,\gamma) = 1 + W_\gamma(R)(1 - \cos(2\gamma)),$$
$$\frac{\partial \Gamma(R,\gamma)}{\partial \gamma} = 2W_\gamma(R)\sin(2\gamma),$$

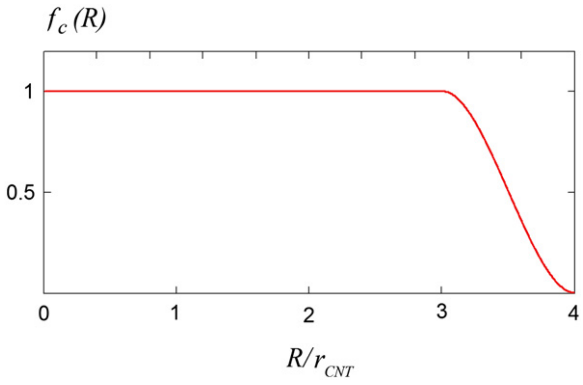

Fig. 16. Cutoff function $f_c(R)$.

$$\begin{aligned}
&\frac{\partial^2\Gamma(R,\gamma)}{\partial^2\gamma} = 4W_\gamma(R)\cos(2\gamma),\\
&\frac{\partial\Gamma(R,\gamma)}{\partial R} = \frac{\partial W_\gamma(R)}{\partial R}(1-\cos(2\gamma)),\\
&\frac{\partial^2\Gamma(R,\gamma)}{\partial^2 R} = \frac{\partial^2 W_\gamma(R)}{\partial^2 R}(1-\cos(2\gamma)),
\end{aligned} \tag{37}$$

$$\begin{aligned}
&W_\gamma(R) = C_\gamma(R/r_{CNT})^\delta,\\
&\frac{dW_\gamma(R)}{dR} = \frac{\delta C_\gamma}{r_{CNT}}(R/r_{CNT})^{\delta-1},\\
&\frac{d^2W_\gamma(R)}{d^2R} = \frac{\delta(\delta-1)C_\gamma}{r_{CNT}^2}(R/r_{CNT})^{\delta-2}.
\end{aligned} \tag{38}$$

The smooth cutoff function $f_c(R)$ (Fig. 16) and its derivatives have the following shape:

$$\begin{aligned}
&f_c(R) = 1, \quad \frac{df_c(R)}{dR} = 0, \quad \frac{d^2f_c(R)}{d^2R} = 0, \quad R < R_{beg}\\
&f_c(R) = Q_0 + Q_1R + Q_2R^2 + Q_3R^3,\\
&\frac{df_c(R)}{dR} = Q_1 + 2Q_2R + 3Q_3R^2,\\
&\frac{d^2f_c(R)}{d^2R} = 2Q_2 + 6Q_3R, \quad R_{beg} < R < R_{end},
\end{aligned} \tag{39}$$

where the coefficients Q_0, Q_1, Q_2, Q_3 are such that

$$f_c(R_{beg}) = 1, \quad f_c(R_{end}) = 0, \quad \left.\frac{df_c(R)}{dR}\right|_{R_{beg}} = 0, \quad \left.\frac{df_c(R)}{dR}\right|_{R_{end}} = 0 \tag{40}$$

they are found from

$$\begin{pmatrix} Q_0\\ Q_1\\ Q_2\\ Q_3 \end{pmatrix} = \begin{pmatrix} 1 & R_{beg} & R_{beg}^2 & R_{beg}^3\\ 1 & R_{end} & R_{end}^2 & R_{end}^3\\ 0 & 1 & 2R_{beg} & 3R_{beg}^2\\ 0 & 1 & 2R_{end} & 3R_{end}^2 \end{pmatrix}^{-1} \begin{pmatrix} f_c(R_{beg})\\ f_c(R_{end})\\ \left.\frac{df_c(R)}{dR}\right|_{R_{beg}}\\ \left.\frac{df_c(R)}{dR}\right|_{R_{end}} \end{pmatrix}. \tag{41}$$

The values of the R_{beg} and R_{end} are as follows:

$$R_{beg}^u = 3r_{CNT}, \quad R_{end}^u = 4r_{CNT}.$$

Fast calculation of trigonometric functions in expressions for $\Theta^k(\theta)$ and its derivatives utilizes particular case of recursive Chebyshev formulas ($i = 1 \ldots k-1$):

$$\begin{aligned}
&\cos 2(i+1)\theta = \cos 2i\theta\cos 2\theta - \sin 2i\theta\sin 2\theta,\\
&\sin 2(i+1)\theta = \sin 2i\theta\cos 2\theta + \cos 2i\theta\sin 2\theta.
\end{aligned} \tag{42}$$

References

Anderson, T., Akatyeva, E., Nikiforov, I., Potyondy, D., Ballarini, R., Dumitrică, T., 2010. Toward distinct element method simulations of carbon nanotube systems. J. Nanotechnol. Eng. Med. 1, 0410009.

Buehler, M.J., 2006. Mesoscale modeling of mechanics of carbon nanotubes: self-assembly, self-folding, and fracture. J. Mater. Res. 21, 2855–2869.

Bulicek, M., Malek, J., Rajagopal, K.R., 2012. On Kelvin–Voigt model and its generalizations. Evol. Equations Control Theory 1, 17–42.

Carlson, A., Dumitrică, T., 2007. Extended tight-binding potential for modelling intertube interactions in carbon nanotubes. Nanotechnology 18, 065706.

Cranford, S.W., Buehler, M.J., 2010. In silico assembly and nanomechanical characterization of carbon nanotube buckypaper. Nanotechnology 21, 265706–265712.

Cundall, P.A., Strack, O., 1979. A discrete numerical model for granular assemblies. Geotechnique 29, 47–65.

Cundall, P.A., Strack, O., 1988. Formulation of a three-dimensional distinct element model. part i: a scheme to detect and represent contacts in a system composed of many polyhedral blocks. Int. J. Rock Mech. Min. Sci. Geomech. Abstr. 25, 107–116.

Dalton, A.B., Collins, S., Munoz, E., Razal, J.M., Ebron, V.H., Ferraris, J.P., Coleman, J.N., Kim, B.G., Baughman, R.H., 2003. Super-tough carbon-nanotube fibers. Nature 423, 703.

Desbrun, M., Gascuel, M.-P. 1996. Smoothed particles: a new paradigm for animating highly deformable bodies. In: Proceedings of EG Workshop on Computer Animation and Simulation 96. Springer-Verlag, pp. 61–76.

Dumitrică, T., Belytschko, T., Yakobson, B.I., 2003. Bond-breaking bifurcation states in carbon nanotube fracture. J. Chem. Phys. 118, 9485.

Dumitrică, T., Yakobson, B.I., 2004. Strain-rate and temperature dependent plastic yield in carbon nanotubes from ab initio calculations. Appl. Phys. Lett. 84, 2775.

Dumitrică, T., Hua, M., Yakobson, B.I., 2006. Symmetry, time, and temperature dependent strength of carbon nanotubes. Proc. Natl. Acad. Sci. U.S.A. 103, 6105–6109.

Dutt, M., Hancock, B., Bentham, C., Elliott, J., 2005. An implementation of granular dynamics for simulating frictional elastic particles based on the DL_POLY code. Comput. Phys. Commun 166, 26–44.

Dzyaloshinskii, I.E., Lifshitz, E.M., Pitaevskii, L., 1961. General theory of van der Waals' forces. Sov. Phys. Usp. 4, 153.

Ensing, B., Nielsen, S., 2010. Multiscale molecular dynamic and the reverse mapping problem. In: Dumitrică, T. (Ed.), Trends in Computational Nanomechanics. Springer Inc., Dordrecht, Heidelberg, London, New York, pp. 25–59.

Filleter, T., Yockel, S., Naraghi, M., Paci, J.T., Compton, O.C., Mayes, M.L., Nguyen, S.T., Schatz, G.C., Espinosa, H.D., 2012. Experimental–computational study of shear interactions within double-walled carbon nanotube bundles. Nano Lett. 12, 732–742.

Gingold, R.A., Monaghan, J.J., 1977. Smoothed particle hydrodynamics: theory and application to non-spherical stars. Mon. Not. R. Astron. Soc. 181, 375–389.

Hahm, M.G., Wang, H., Jung, H., Hong, S., Lee, S.G., Kim, S.R., Upmanyu, M., Jung, Y.J., 2012. Bundling dynamics regulates the active mechanics and transport in carbon nanotube networks and their nanocomposites. Nanoscale 1, 1–8.

Hamaker, H.C., 1937. The London–van der Waals attraction between spherical particles. Physica 4, 1058–1072.

Harris, J.M., Iyer, G.R.S., Bernhardt, A.K., Huh, J.Y., Hudson, S.D., Fagan, J.A., Hobbie, E.K., 2012. Electronic durability of flexible transparent films from type-specific single-wall carbon nanotubes. ACS Nano 6, 881–887.

Hart, R., Cundall, P., Lemos, J., 1988. Formulation of a three-dimensional distinct element model. Part ii: mechanical calculations for motion and interaction of a system composed of many polyhedral blocks. Int. J. Rock Mech. Min. Sci. Geomech. Abstr. 25, 117–126.

Hatami-Marbini, H., Picu, C.R., 2009. Heterogeneous long-range correlated deformation of semiflexible random fiber networks. Phys. Rev. E 80, 046703.

Hobbie, E.K., Simien, D.O., Fagan, J.A., Huh, J.Y., Chung, J.Y., Hudson, S.D., Obrzut, J., Douglas, J.F., Stafford, C.M., 2010. Wrinkling and strain softening in single-wall carbon nanotube membranes. Phys. Rev. Lett. 104, 125505.

Hoover, W., 2006. Smooth Particle Applied Mechanics: The State of the Art. World Scientific.

Huang, X., Zou, J., Zhang, S.L., 2008. Bilinear responses and rippling morphologies of multiwalled carbon nanotubes under torsion. Appl. Phys. Lett. 93, 031915.

Humphrey, W., Dalke, A., Schulten, K., 1996. Vmd—visual molecular dynamics. J. Mol. Graphics 14, 33–38.

Hutchens, S.B., Needleman, A., Greer, J.R., 2012. A microstructurally motivated description of the deformation of vertically aligned carbon nanotube structures. Appl. Phys. Lett. 100, 121910.

Iijima, S., 1991. Helical microtubules of graphitic carbon. Nature 354, 56–58.

Itasca Consulting Group Inc., 2008. PFC3D (Particle Flow Code in 3 Dimensions). Version 4.0. Itasca Consulting Group Inc., Minneapolis.

Jeong, B.W., Lim, J.K., Sinnott, S.B., 2007. Elastic torsional responses of carbon nanotube systems. J. Appl. Phys. 101, 084309.

Liba, O., Kauzlaric, D., Abrams, Z.R., Hanein, Y., Greiner, A., Korvink, J.G., 2008. A dissipative particle dynamics model of carbon nanotubes. Mol. Sim. 34, 737–748.

Liang, H., Upmanyu, M., 2005. Size-dependent intrinsic bulk twisting of carbon nanotube ropes. Carbon 43, 3189–3193.

London, F., 1930. Zur theorie und systematik der molekularkräfte. Z. Phys. 63, 245–279.

Martel, R., Shea, H., Avouris, P., 1999. Rings of single-walled carbon nanotubes. Nature 398, 299.

Nikiforov, I., Zhang, D.-B., James, R.D., Dumitrică, T., 2010. Wavelike rippling in multiwalled carbon nanotubes under pure bending. Appl. Phys. Lett. 96, 123107.

Pande, G., Beer, G., Williams, J.R., 1990. Numerical Modeling in Rock Mechanics. John Wiley and Sons.

Potyondy, D., Cundall, P., 2004. A bonded-particle model for rock. Int. J. Rock Mech. Min. Sci. 41, 1329–1364.

Rajter, R.F., Podgornik, R., Parsegian, A.V., French, R.H., Ching, W.Y., 2007. Van der Waals–London dispersion interactions for optically anisotropic cylinders: metallic and semiconducting single-wall carbon nanotubes. Phys. Rev. B 76, 045417.

Rouse, P.E., 1953. A Theory of the linear viscoelastic properties of dilute solutions of coiling polymers. J. Chem. Phys. 21, 1272–1280.

Rurali, R., Hernandez, E., 2003. Trocadero: a multiple-algorithm multiple-mode atomistic simulation program. Comput. Mater. Sci. 28, 85–106.

Shi, X., Kong, Y., Gao, H., 2008. Coarse grained molecular dynamics and theoretical studies of carbon nanotubes entering cell membrane. Acta Mech. Sin. 24, 161–169.

Shuba, M.V., Paddubskaya, A.G., Plyushch, A.O., Kuzhir, P.P., Slepyan, G.Ya., Maksimenko, S.A., Ksenevich, V.K., Buka, P., Seliuta, D., Kasalynas, I., Macutkevic, J., Valusis, G., Thomsen, C., Lakhtakia, A., 2012. Experimental evidence of localized plasmon resonance in composite materials containing single-wall carbon nanotubes. Phys. Rev. B 85, 165435.

Suhr, J., Koratkar, N., Keblinski, P., Ajayan, P., 2005. Viscoelasticity in carbon nanotube composites. Nat. Mater. 4, 134–137.

Sulsky, D., Zhou, S.-J., Schreyer, H.L., 1994. A particle method for history-dependent materials. Comput. Methods Appl. Mech. Eng. 118, 179.

Tersoff, J., 1988. New empirical approach for the structure and energy of covalent systems. Phys. Rev. B 37, 6991–7000.

Thess, A., Lee, R., Nikolaev, P., Dai, H., Petit, P., Robert, J., Xu, C., Lee, Y.H., Kim, S.G., Rinzler, A.G., Colbert, D.T., Scuseria, G.E., Tomanek, D., Fischer, J.E., Smalley, R.E., 1996. Crystalline ropes of metallic carbon nanotubes. Science 273, 483–487.

Underhill, P.T., Doyle, P.S., 2003. On the coarse-graining of polymers into bead-spring chains. J. Non-Newtonian Fluid Mech. 122, 3–31.

Volkov, A.N., Simov, K.R., Zhigilei, L.V., 2008. Mesoscopic model for simulation of CNT-based materials. In: Proceedings of the ASME International Mechanical Engineering Congress and Exposition, Boston, MA, October 31–November 6, pp. 1–11.

Volkov, A.N., Zhigilei, L.V., 2010a. Mesoscopic interaction potential of carbon nanotubes of arbitrary length and orientation. J. Phys. Chem. C 114, 5513–5531.

Volkov, A.N., Zhigilei, L.V., 2010b. Scaling laws and mesoscopic modeling of thermal conductivity in carbon nanotube materials. Phys. Rev. Lett. 104, 215902.

Volkov, A.N., Zhigilei, L.V., 2010c. Structural stability of carbon nanotube films: the role of bending buckling. ACS Nano 4, 6187–6195.
Wang, H.K., Liu, Y., Zhang, X., 2012. The carbon nanotube composite simulation by material point method. Comput. Mater. Sci. 57, 23–29.
Xie, B., Liu, Y., Ding, Y., Zheng, Q., Xu, Z., 2011. Mechanics of carbon nanotube networks: microstructural evolution and optimal design. Soft Matter 7, 10039–10047.
Zhang, P., Lammert, P.E., Crespi, V.H., 1998. Plastic deformations of carbon nanotubes. Phys. Rev. Lett. 81, 5346–5349.
Zhang, D.B., Dumitrică, T., 2008. Elasticity of ideal single-walled carbon nanotubes via symmetry-adapted tight-binding objective modeling. Appl. Phys. Lett. 93, 031919–031921.
Zhang, D.B., James, R.D., Dumitrică, T., 2009. Electromechanical characterization of carbon nanotubes in torsion via symmetry adapted tight-binding objective molecular dynamics. Phys. Rev. B 80. 115418–115415.
Zhang, X.Q., Li, Q., Tu, Y., Li, Y., Coulter, J.Y., Zheng, L., Zhao, Y., Jia, Q., Peterson, D.E., Zhu, Y., 2007. Strong carbon-nanotube fibers spun from long carbon-nanotube arrays. Small 3, 244.
Zhigilei, L.V., Wei, C., Srivastava, D., 2005. Mesoscopic model for dynamic simulations of carbon nanotubes. Phys. Rev. B 71, 165417–165428.
Zimm, B.H., 1956. Dynamics of polymer molecules in dilute solution: viscoelasticity, flow birefringence and dielectric loss. J. Chem. Phys. 24, 269–278.
Zou, J., Huang, X., Arroyo, M., Zhang, S., 2009. Effective coarse-grained simulations of superthick multiwalled carbon nanotubes under torsion. J. Appl. Phys. 105, 033516.